CHEMISTRY

Electrically polarized nanoscale surfaces generate reactive oxygenated and chlorinated species for deactivation of microorganisms

Annie Y. Vargas-Lizarazo¹†, M. Aswad Ali¹†, Nehal A. Mazumder¹, Gitanjali M. Kohli², Miroslava Zaborska¹, Tyler Sons³, Michelle Garnett³, Ishani M. Senanayake¹, Boyd M. Goodson¹, José M. Vargas-Muñiz³, Amber Pond⁴, Philip J. Jensik⁵, Michael E. Olson⁶, Scott D. Hamilton-Brehm³, Punit Kohli^{1,7}*

Because of the decreasing supply of new antibiotics, recent outbreaks of infectious diseases, and the emergence of antibiotic-resistant microorganisms, it is imperative to develop new effective strategies for deactivating a broad spectrum of microorganisms and viruses. We have implemented electrically polarized nanoscale metallic (ENM) coatings that deactivate a wide range of microorganisms including Gram-negative and Gram-positive bacteria with greater than 6-log reduction in less than 10 minutes of treatment. The electrically polarized devices were also effective in deactivating lentivirus and *Candida albicans*. The key to the high deactivation effectiveness of ENM devices is electrochemical production of micromolar cuprous ions, which mediated reduction of oxygen to hydrogen peroxide. Formation of highly damaging species, hydroxyl radicals and hypochlorous acid, from hydrogen peroxide contributed to antimicrobial properties of the ENM devices. The electric polarization of nanoscale coatings represents an unconventional tool for deactivating a broad spectrum of microorganisms through in situ production of reactive oxygenated and chlorinated species.



Copyright © 2024 me
Authors, some rights
reserved; exclusive
licensee American
Association for the
Advancement of
Science. No claim to
original U.S.
Government Works.
Distributed under a
Creative Commons
Attribution
NonCommercial
License 4.0 (CC BY-NC).

INTRODUCTION

Consistent attention is aimed at communicable diseases, which are identified as a key challenge to public health and are also recognized as a major concern for global welfare (1). It is estimated that, of 13.7 million infection-related deaths in 2019, about 7.7 million deaths were associated with 33 bacterial pathogens (2). Recent multiple outbreaks of infectious diseases, including severe acute respiratory syndrome coronavirus 2 (3-5), Mpox (6, 7), influenza A (widespread yearly outbreak) (8-10), measles morbillivirus (11, 12), and various bacterial infections (3), have resulted in an enormous loss of human lives, causing substantial adverse impacts on the global economy and society. Furthermore, the rapid rise of antimicrobial resistance (AMR) poses an urgent and grave threat, adding to a substantial clinical and financial burden on health care systems (13–18). Thus, there is an urgent and pressing need to develop new tools, methods, and strategies that are effective against a broad range of microorganisms, viruses, and protozoans (19-22).

A number of antimicrobial approaches involving biological, small, and large organic molecules and metallic nanoscale materials have been implemented in the literature. For example, peptides (19, 20, 23–25), enzymes (19, 20, 24), bacteriophages (19, 20), organic biocides (13, 19, 20, 22, 24), small-molecule inhibitors (19, 26, 27), and high-molecular weight polymers (19, 28, 29) have shown promise

against many infection-causing viruses and microorganisms. Metallic nanoparticles (NPs) and coatings are also extensively investigated for antimicrobial applications. Silver (19, 21, 30–33), gold (34–38), copper (19, 27, 32), CuO (19, 27, 39, 40), MgO (41), Fe₂O₃ (42), TiO₂ (43, 44), CeO₂ (45), and ZnO (19, 39, 40, 45, 46) are demonstrated in deactivating microorganisms and viruses.

In general, organic antibiotics and biological-based antimicrobial species deactivate bacteria through one or more action of mechanisms, by interrupting or inhibiting crucial bacterial biochemical and biophysical pathways; adversely disrupting the mechanical integrity of the cells (for example, cell wall/membrane); and forming pores in the membrane (19). Similarly, the antimicrobial properties of the metal-based materials are thought to be due to multiple modes of mechanisms, including generation of oxidative species (21, 42, 47–49), release of metallic ion contributing to cell toxicity (19, 24, 30, 47, 48), mechanical damage to cell/membrane wall, and suppression of the antioxidant response of the host cell (19, 30, 42, 47, 48). Depending on the concentration of oxidative and other toxic species, the host cell cycle could be severely affected and inhibited, or even apoptosis (programmed cell death process) could be activated (50–55).

Recently, nanoscale materials and surfaces exhibiting exciting deactivation mechanisms against microorganisms and viruses have been reported (36–38, 56–62). Rotello's group recently demonstrated ligand-engineered NPs, which exhibit potent antimicrobial activities against multidrug-resistant bacteria (36–38). Thioxanthene-based light-activated molecular machines showed excellent antibacterial properties that rapidly kill a broadband of bacteria including drugresistant microbes by disrupting bacterial membranes (58, 63). Photoactive biocidal molecules containing nanofibrous membranes produced reactive oxygenated species (ROS) that deactivated bacteria and viruses with more than 6-log difference (57). Similarly, photocatalytic-based nanoscale films (19–21), nanotextured silicon films (64), zwitterion polymer films (65), synergetic quantum dot–antibiotic nanoscale

¹School of Chemical and Biomolecular Sciences, Southern Illinois University, Carbondale, IL 62901, USA. ²Carbondale High School, Carbondale, IL 62901, USA. ³Department of Microbiology, Southern Illinois University, Carbondale, IL 62901, USA. ⁴Department of Anatomy, Southern Illinois University School of Medicine, Carbondale, IL 62901, USA. ⁵Department of Physiology, Southern Illinois University School of Medicine, Carbondale, IL 62901, USA. ⁶Department of Medical Microbiology, Immunology and Cell Biology, School of Medicine, Southern Illinois University, Springfield, IL 62702, USA. ⁷Integrated Microscopy and Graphics Expertise (IMAGE) Center, Southern Illinois University, Carbondale, IL 62901, USA.

^{*}Corresponding author. Email: pkohli@chem.siu.edu

[†]These authors contributed equally to this work.

materials (66), and silver-containing polymers (59, 67) have shown great promises against many microorganisms, including antibiotic-resistant bacteria (36, 38, 58). However, some concerns such as rechargeability, toxicity, and stability of the active species contribute to their reduced applicability and usages (19, 24).

Here, we report that electrically polarized nanoscale metallic (ENM) coatings, composed of Cu(II) and Ag, deactivate and kill both Gram-positive and Gram-negative bacteria with more than 6-log reduction in less than 10 min of treatment. The electric polarization of the coatings was accomplished using low-power alkaline batteries or solar cells. ENM devices were rationally designed for the in situ production of micromolar cuprous ions in solutions for an extended period of time (>2 days). The cuprous ions are implicated in the production of ROS, (hydrogen peroxide and hydroxyl radicals), reactive chlorinated species (RCS), including hypochlorous acid. Highly damaging ROS and RCS produced by the ENM devices also deactivated broad-spectrum microorganisms including medically relevant Pseudomonas aeruginosa, Acinetobacter baumannii, and Staphylococcus aureus with an efficiency of $\approx 99.9999\%$ (more than 6-log reduction). ENM devices were also effective against Candida albicans fungal spores with an efficiency of $\approx 93\%$. Treating lentivirus with electrically polarized metallic coatings resulted in >90% deactivation of the virus. ENM devices are easy to fabricate in a short time (<2 hours) using accessible materials on a variety of flexible wearable surfaces. Furthermore, the microorganism deactivation efficiency was "actively" modulated by the magnitude of applied potential to the devices. The electrical polarization of the nanoscale metallic surfaces represents an unconventional tool for deactivating microorganisms and viruses through in situ production of ROS and RCS. Overall, these studies contribute to addressing current challenges of managing and reducing the spread of infectious diseases by implementing electrically polarized, self-sanitizing, nanoscale materials.

RESULTS

Fabrication and characterization of ENM devices

Figure 1A shows a schematic of implementation of the ENM devices for the deactivation of microorganisms and viruses. Briefly, an aqueous drop, represented by a large transparent light blue sphere, containing three healthy microorganisms (rose-, green-, and pistachio-colored structures), was placed on a control device (white rectangle) (Fig. 1A). The control treatment did not exhibit any damage or deactivation of the microorganisms (Fig. 1A, top). The microorganisms were, however, deactivated with a greater than 6-log reduction after they were treated with an ENM device for less than 10 min. The damaged microorganisms are represented by perforated structures in the bottom figure of Fig. 1A. The deactivation of the microorganisms was caused by ROS (shown by smaller cyan and red spheres) and RCS (light pink sphere), which were produced by electrically polarized metallic nanoscale coatings (dark gray rectangle). The electrical polarization of the devices was accomplished by either alkaline batteries or commercial solar cells irradiated with a light-emitting diode (LED). (–) and (+) in Fig. 1A represent – and + polarities of a source battery, respectively. Electrically polarized ENM devices with $E_{app} = 3$ and 6 V are referred to as ENM_{3V} and ENM_{6V}, respectively, whereas the electrically nonpolarized ENM devices ($E_{app} = 0 \text{ V}$) are denoted by ENM_{0V}.

The ENM devices were fabricated using a simple two-step process (Fig. 1B). First, the polypropylene control surfaces were immersed in a 0.1 M CuSO₄ solution for 1 hour (Fig. 1B and figs. S1 and S2), yielding

an average copper concentration of ([Cu(II)]) ≈ 15.7 parts per million (ppm) cm⁻² (n = 4) on the surfaces (fig. S3). Then, 80- to 100-nm-thick coating of silver was sputtered on both sides of the Cu-containing surfaces (Fig. 1, G and H). The silver coating is composed of NPs of 29 \pm 5 nm (n = 172) (Fig. 1I). A typical ENM device is shown in Fig. 1C. ENM devices were also fabricated on a variety of surfaces, including household air filters, cellulose filter paper, and hand paper towels. A detailed procedure for the fabrication of ENM devices is provided in the Supplementary Materials.

Energy-dispersive x-ray spectroscopy (EDS) confirmed the presence of elemental Cu (L_α 0.930 keV and K_α 8.04 keV) and Ag (L_α 2.984 keV) on ENM devices (Fig. 1, D and E, figs. S5 to S9, and table S2). The sheet resistances (R_s) of the freshly prepared ENM devices and after five usages were 32 ± 12 ohm cm⁻² (n = 6) and 129 ± 132 ohm cm⁻² (n = 6), respectively (fig. S11). The water static contact angles (θ_c) on the ENM devices (E_{app} = 3 V) were 118° ± 7° and 115° ± 6° (n = 3) for ENM treatment durations (τ_{app}) of 0 and 10 min, respectively (Fig. 1F and fig. S10). The observed change in θ_c was insignificant for ENM_{0V} and ENM_{3V} treatments for τ_{app} = 10 min (fig. S10).

Rationale for electrically polarized metallic surfaces for ROS and RCS generation

Before describing antimicrobial and antiviral properties of ENM devices, we provide a rationale of electrical polarization of the nanoscale copper-silver metallic coatings for the generation of ROS and RCS. ENM treatments produced H₂O₂, which decomposed to *OH through Fenton-like reaction (68), although recently, other oxidative species are also implicated in the Fenton-like reaction (69). Furthermore, HOCl was also produced in the solutions treated with ENM devices through a reaction between H₂O₂ and Cl⁻ (70). Both *OH and HOCl are known to be highly damaging to cells (50) and are attributed to deactivation of microorganisms and lentivirion with ENM treatments.

The first step for the generation of ROS and RCS in an ENMtreated solution is Cu(I)-mediated O2 reduction to O2., which is followed by a second one-electron reduction of $O_2^{\bullet-}$ to H_2O_2 . Cu(I)mediated reduction of O₂ to O₂ has a standard reduction potential (E_0) of -0.319 V (Supplementary Materials); thus, it exhibits a thermodynamic limitation. This limitation is, however, strictly applied to thermodynamic equilibrium conditions and can be kinetically relaxed, as is evident from multiple reports demonstrating the feasibility of Cu(I)-mediated O_2 reduction to $O_2^{\bullet -}$ (71–75). Cu(II) to Cu(I) reduction is thought to occur under dynamic nonequilibrium conditions in sunlit seawater, where submicromolar to nanomolar Cu(I) concentration exists (71). Although O₂ reduction and O₂ oxidation mediated by copper species can involve multiple reaction pathways (eqs. S1 to S9, Supplementary Materials), it may be useful to consider them as a two-step reaction (Eq. 1). These considerations provide useful insights and rationale concerning the kinetics of Cu(I)mediated O₂ reduction to O₂.

$$O_2 + Cu(I) \underset{k}{\overset{k_f}{\rightleftharpoons}} O_2^{\bullet -} + Cu(II) \underset{reactant}{\overset{k}{\Rightarrow}} Products$$
 (1)

where k_f , k_r , and k are rate constants. $k_f = 3.1 \times 10^4 \text{ M}^{-1} \text{ s}^{-1}$, $k_r = 6.6 \times 10^8 \text{ M}^{-1} \text{ s}^{-1}$, and k varies with reactants and reaction conditions (73).

We evaluate kinetic feasibility of Cu(I)-mediated O_2 reduction to $O_2^{\bullet-}$ by estimating a kinetic parameter (R_{kin}) for the ENM system.

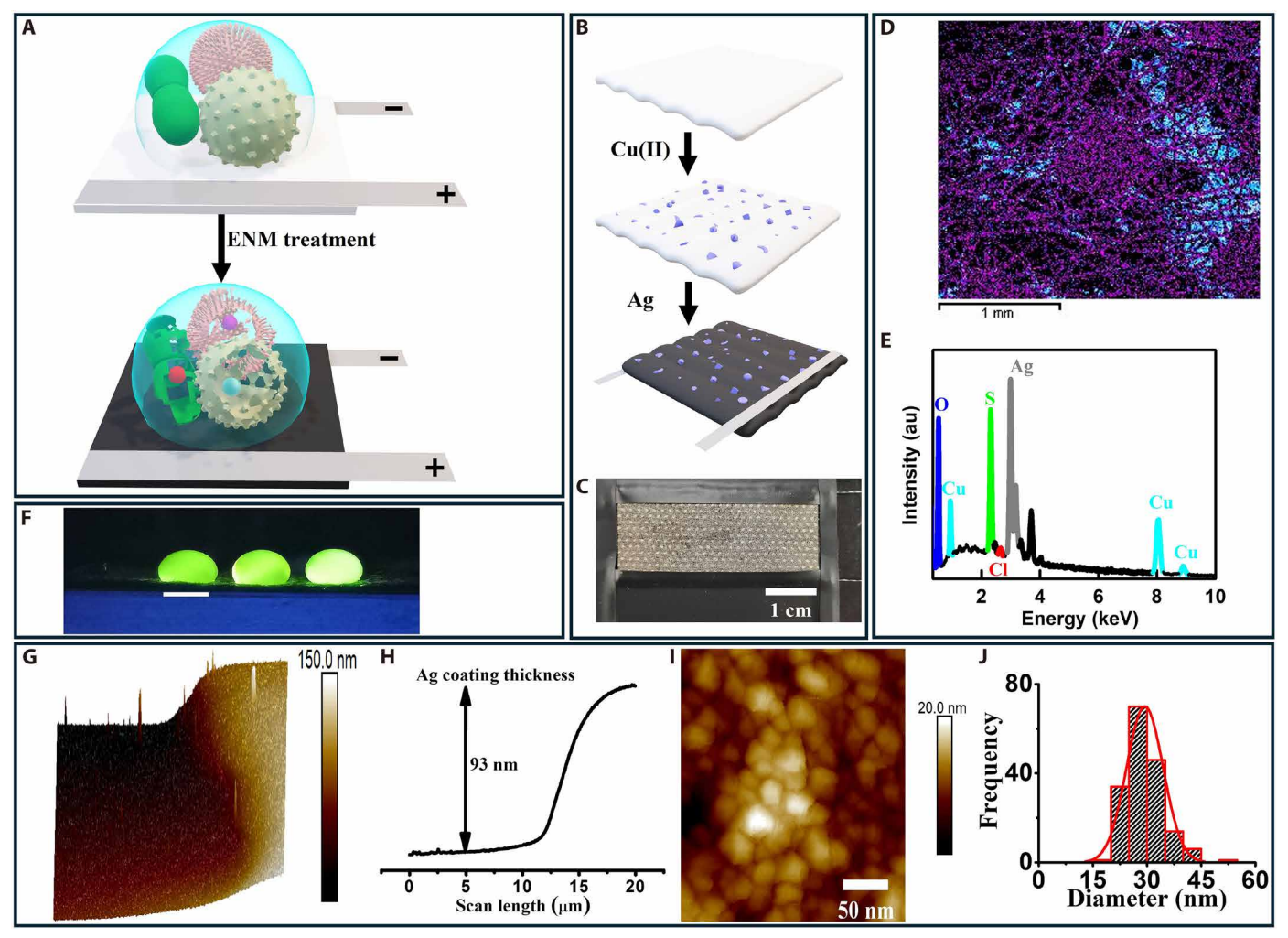


Fig. 1. Working principle, fabrication, and characterization of the ENM devices. (A) Top (control treatment): An aqueous droplet (large light blue sphere), containing three healthy microorganisms (represented by rose-, green-, and pistachio-colored structures), was placed on a control device (white rectangle with two strips). Bottom (ENM treatment): The microorganisms were deactivated in less than 10 min of ENM treatment. The perforation of these three structures represents damage and deactivation of the microorganisms. The (+) and (-) represent + and - polarities of a battery, respectively. 'OH, H_2O_2 , and HOCl are represented by cyan, red, and light pink spheres, respectively. (B) ENM fabrication involves the deposition of Cu(II) (blue particles) on a substrate (white rhombus) by immersion in a 0.1 M CuSO₄ solution followed by ~90-nm silver coating (dark gray). (C) Optical image of a typical ENM device. (D) EDS mapping of an ENM device, showing Cu (blue) and Ag (purple). (E) An EDS energy spectrum on ENM revealed the presence of elements C, O, S, Cl, Cu, and Ag. au, arbitrary units. (F) Fluorescence micrograph of three 40 μ M fluorescein-containing water droplets deposited on ENM₃y for $\tau_{app} = 10$ min, exhibiting a water contact angle of $\approx 115 \pm 6^{\circ}$ (n = 3). Scale bar, 5 mm. AFM measurements: (G) Two-dimensional AFM scan of silver coating on glass yielded a thickness of ≈ 93 nm (H); (J) histogram of the silver particle size in (I) exhibited an average silver particle size of 29 ± 5 nm (n = 172).

 $[O_2] \approx 254 \, \mu M$ (76) in an air-saturated solution is about eight to nine orders of magnitude larger than that of steady-state $[O_2^{\bullet -}]$ (14 to 234 pM, Supplementary Materials). Thus, $R_{\rm kin} = \frac{k_{\rm f}[O_2][{\rm Cu}(I)]}{k_{\rm f}[O_2^{\bullet -}][{\rm Cu}(II)]} \gg 1$ indicates that the forward reaction is kinetically accessible (Supplementary Materials). Furthermore, the reaction of $O_2^{\bullet -}$ with species such as Cu(I) present in the solution is fast ($k = 2 \times 10^9 \, {\rm M}^{-1} \, {\rm s}^{-1}$), facilitating O_2 reduction in the forward direction.

Another possibility for the generation of H_2O_2 is through a two-electron reduction of O_2 to H_2O_2 by two Cu(I) species (77, 78). Although the reaction $2Cu(I) + O_2 + 2H^+ \rightarrow H_2O_2 + 2Cu(II)$ is thermodynamically viable ($E_0 = 0.436 \text{ V}$) (79), it imposes a spatial restriction of availability of two Cu(I) species in close vicinity during the reaction. In any case, Cu(I) is known to play a crucial role in the generation of H_2O_2 .

Here, we rationally designed surfaces and devices that produced Cu(I) using two modes: First, Cu(I) was generated by electrically polarizing nanoscale Cu(II)-Ag coatings with low-power alkaline batteries or solar cells through Cu(II) reduction to Cu(I). Cu(II) \rightarrow Cu(I) is known to occur in Cu(II)-containing aqueous solutions under an appropriate electric potential (80). Second, the Walden reductor was implemented for Cu(II) \rightarrow Cu(I) ($E_{\rm o}=0.159$ V). The Walden reductor provided an appropriate reduction potential of $E_{\rm o,Walden}=0.2305$ V to achieve Cu(II) \rightarrow Cu(I). However, it does not allow Cu(II) \rightarrow Cu(0) ($E_{\rm o}=0.3419$ V), which is larger than $E_{\rm o,Walden}$ (81, 82). Although only the Walden reductor generated Cu(I) in the absence of an applied potential to the ENM devices (referred to as ENM_{0V}), Cu(I) was generated by both modes in the presence of $E_{\rm app}=3$ V (referred to as ENM_{3V}).

Rapid broadband microbial deactivation by ENM

We worked with seven different microorganisms from two different kingdoms: five bacteria (both Gram-positive and Gram-negative), two fungi, and one virus (lentivirus). Three human-health relevant bacteria—A. baumannii, P. aeruginosa, and S. aureus [a part of the ESKAPE family (83)]—were chosen for deactivation investigations by ENM devices. These bacteria are considered excellent bacterial models of nosocomial opportunistic pathogens that cause infections with high morbidity and mortality (84-86). These bacteria are known to escape biocidal actions of common antibiotics, leading to development of antibiotic-resistant bacteria (83). S. aureus is the leading cause of bacterial death in 135 counties and is also associated with the most mortality rate among individuals 15 years and older (2). Two extremophiles, SIUC2 [a Gram-negative, 85% identification (ID) to Serratia marcescens] and SIUC11 (a Gram-positive, 99% ID to Bacillus safensis), were also used in our studies (Supplementary Materials). Furthermore, two fungi, Aspergillus fumigatus (strain ΔakuB^{KU80}) and C. albicans (strain SC5314, American Type Culture Collection MYA-2876), were also used to evaluate antimicrobial properties of ENM devices. These fungi are known to cause diseases in immunodeficient humans. Lastly, antiviral properties of the devices were examined against lentivirus, which is a model virus used in biomedical studies.

Briefly, three to six 100-µl droplets containing a known concentration of a desired microorganism or lentivirus were placed on ENM_{0V} and ENM_{3V} devices. The treatment time (τ_{app}) for the studies was 5 min, unless otherwise stated. The sample droplets formed bead-like structures on the devices (Fig. 1F and fig. S10), allowing accurate extraction of $\approx 91 \pm 4 \,\mu l$ (n = 72) for culture growth studies. Approximately 7.5% of viable A. fumigatus were retained on both control and ENM devices for $\tau_{app} = 5$ min treatments. This was considered in our analysis by assuming that 7.5% of the initial concentration of the microorganisms and lentivirion was retained on the devices. The treated microorganisms were then grown in culture media for 24 hours. The device-treated lentivirion were transduced into human embryonic kidney (HEK) 293T cells to evaluate the device deactivation efficiency against lentivirion. The viable microorganism population was manually counted and is reported as an average \pm SD $(n \ge 3)$. The deactivation efficiency (η) and log reduction in the population of microorganisms for different treatments were estimated using Eqs. 2 and 3, respectively:

$$\eta = \frac{\text{CFU}_{\text{control}} - \text{CFU}_{\text{device}}}{\text{CFU}_{\text{control}}} \times 100$$
 (2)

$$\Delta \log = \log(CFU_{control}) - \log(CFU_{device})$$
 (3

of a given bacteria on control and device treatment, respectively. The Δ log represents mean log reduction in the microorganism population treated with control as compared to population of microorganisms treated with a device. For lentivirus studies, $\eta = \left(1 - \frac{I_i}{I_i}\right) \times 100$, where I_i is the fluorescence emission intensity of the healthy HEK293T mammalian cells that were transduced with control surface treated lentivirion. I_f is the fluorescence emission intensity of the HEK293T cells that were transduced with Ag device-treated lentivirion.

where CFU_{control} and CFU_{device} are mean colony-forming units ml⁻¹

Figure 2 shows deactivation of a SIUC2 and SIUC11 mixture (50% each) treated with six devices at $E_{\rm app} = 0$ and 3 V ($\tau_{\rm app} = 5$ min, n = 3).

The Δ log values of the cells treated with devices composed of Cu(II), Ag, Au, and Cu(II)/Au were either insignificant or relatively modest in magnitude (Fig. 2B). These experiments indicated that the presence of Cu(II) by itself with $E_{app} = 3 \text{ V}$ [$\Delta \log = 0.004$, P = not significant(ns) versus control] and 0 V ($\Delta \log = -0.015$, P = ns versus control) on electrically nonconductive surfaces was not effective in deactivating SIUC2 and SIUC11 bacterial cells (Fig. 2). Similarly, for electrically conductive Au- and Ag-functionalized devices at $E_{app} = 3 \text{ V}$ but without Cu(II) yielded a modest $\Delta \log = (0.176 \pm 0.029)$ and (0.571 ± 0.340) , respectively (Table 1). These results suggested that the electric polarization of the electric conductive devices that did not contain Cu(II) was modestly effective against SIUC2-SIUC11 bacteria. The experiments conducted with ENM_{0V} exhibited $\Delta \log = 1.96 \pm 0.360$ (n = 3, P < 0.0001) for the SIUC2-SIUC11 bacterial cells. However, the viable SIUC2-SIUC11 cells were not detected (referred to as ND) for all experiments (n > 50) when the bacterial cells were treated with ENM_{3V} (Fig. 2, figs. S12 and S14, and Table 1). Furthermore, ENM_{3V} treatments ($\tau_{app} = 10$ to 15 min) of SIUC2-SIUC11 at a much higher load of $[C_0] = 5 \times 10^7$ CFU ml⁻¹ did not exhibit viable cells (i.e., CFU $ml^{-1} = 0$) after a 24-hour growth period (fig. S14). These studies further reinforced that the ENM devices are capable of deactivating a higher load of bacteria with $\Delta \log \approx 7.7$ and $\eta \approx 99.99999\%$ in 15 min of treatment. Last, the SIUC2-SIUC11 mixture treated with Cu(II)-Au devices at $E_{app} = 0$ and 3 V exhibited modest $\Delta \log = 1.04 \pm 0.141$ and 1.23 \pm 0.131, respectively (Fig. 2, fig. S13, and table S3). These experiments confirmed that the electric polarization of the coatings composed of cupric ions and nanoscale silver plays a crucial role in the antimicrobial properties of the devices. As shown below, the high deactivation efficiency of the ENM devices against microorganisms and lentivirion is due to generation of ROS and RCS, which react with cellular and virus components resulting in the irreversible damage of these species.

The ENM_{0V} treatment exhibited a modest $\Delta \log = 0.07$ (P < 0.0001versus control) and 0.028 (P < 0.0001 versus control) for P. aeruginosa and A. baumannii, respectively. On the other hand, the viable P. aeruginosa and A. baumannii cells in the culture growth media were not detected for ENM_{3V} treatment, which corresponds to $\Delta \log = 6.18$ and 6.48, respectively (P < 0.0001 versus control, n = 3; Fig. 3 and Table 1). S. aureus cells were, however, found to be more resistant, exhibiting modest $\eta \approx 89\%$ ($\Delta \log = 0.94$) and 99.8% ($\Delta \log = 2.75$) (P < 0.05 versus control, n = 3) for ENM_{0V} and ENM_{3V} treatments, respectively ($\tau_{app} = 5$ min). Thus, more aggressive treatments comprising ENM_{6V} and $\tau_{app} = 10$ min were performed, which resulted in a complete deactivation of S. aureus ($\Delta \log = 6.4$, P < 0.0001 versus control; Fig. 3C and Table 1). All five bacteria investigated in the studies were deactivated by ENM_{3V} (or ENM_{6V}) treatments with $\eta \approx 99.9999\%$ ($\Delta \log > 6$). The antimicrobial effectiveness of the ENM devices against two fungi (C. albicans and A. fumigatus) was also studied. Ninety microliters of the fungal spores treated with ENM devices was grown in a culture media for 24 hours. Although the ENM_{3V} treatment successfully deactivated C. albicans with $\eta = 93\%$ (P < 0.0001), the ENM_{0V} treatment exhibited $\eta = 80\%$ (P < 0.0001); Table 1). In comparison, the *C. albicans* deactivation efficiency of the Cu(II)- and Ag-treated devices were 17.4 and 14.7%, respectively (table S4). However, the ENM $_{0V}$ treatment against A. fumigatus spores yielded a modest $\eta \approx 47\%$ $(\tau_{app}=10$ min), but it increased to 92% with ENM_{9V} ($\tau_{app} = 10$ min; fig. S15). Thus, η for A. fumigatus treated with ENM devices was significantly lower than that was observed for bacterial deactivation efficiency (99.9999%) even when A. fumigatus

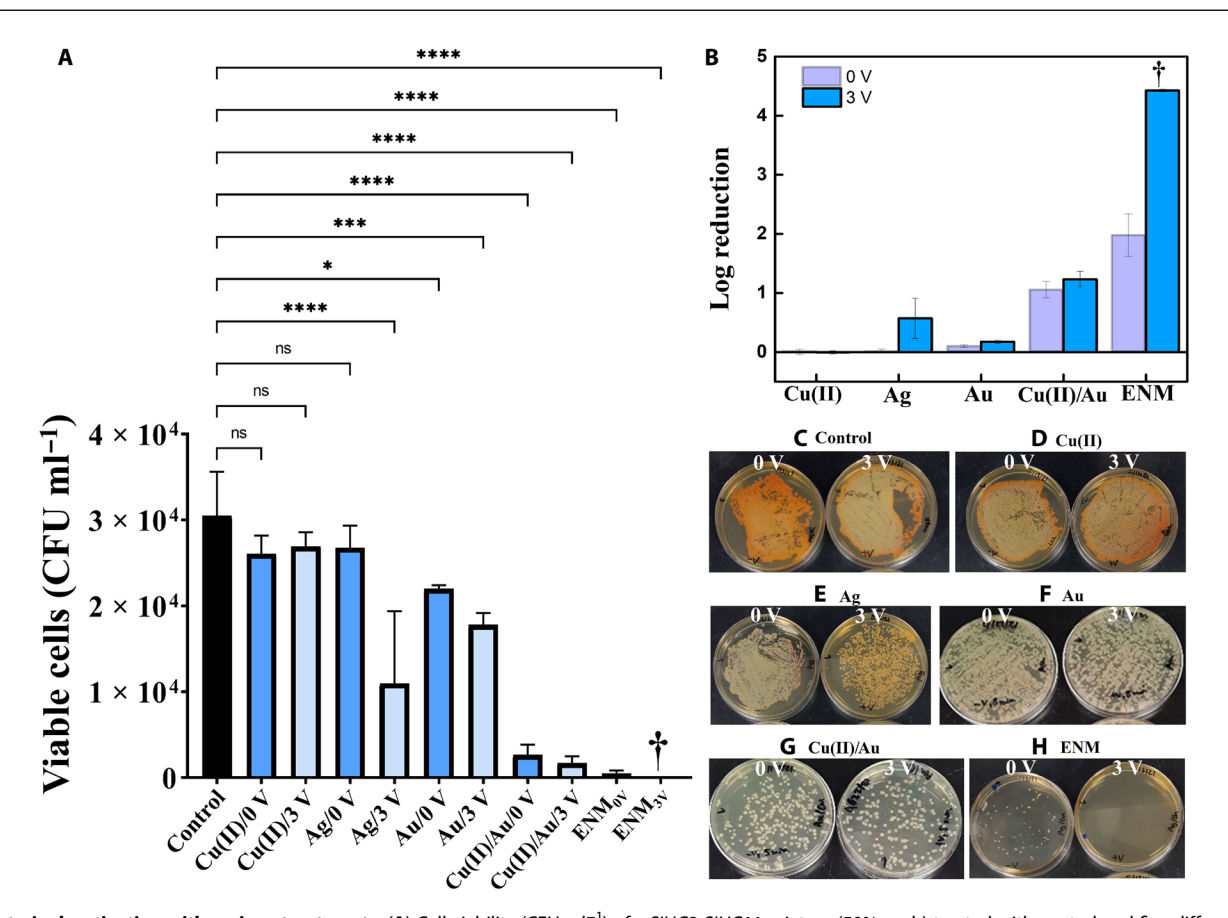


Fig. 2. Bacteria deactivation with various treatments. (**A**) Cell viability (CFU ml⁻¹) of a SIUC2-SIUC11 mixture (50% each) treated with control and five different devices without ($E_{app} = 0 \text{ V}$) and with applied potential ($E_{app} = 3 \text{ V}$). ns: *P* is not significant versus control, *P = 0.0186 versus control, ***P = 0.0003 versus control, and ****P < 0.0001 versus control. The bars represent the arithmetic mean of the data, and the error bars represent the SD of three independent experiments. "0 V" and "3 V" on the *x* axis mean that $E_{app} = 0$ and 3 V, respectively. (**B**) Log reduction for the SIUC2 and SIUC11 mixture treated with five different devices at $E_{app} = 0 \text{ V}$ (purple bars) and 3 V (blue bars). † in (A) and (B) denotes that vial bacterium was not detected for the ENM_{3V} treatment. The optical micrographs of growth of the SIUC2 and SIUC11 mixture treated with control (**C**), Cu(II) device (**D**), Ag device (**E**), Au device (**F**), Cu(II)/Au device (**G**), and ENM device (**H**) at $E_{app} = 0 \text{ and } 3 \text{ V}$. Additional optical micrographs showing bacteria growth on various devices for three independent experiments are available in figs. S12 and S13. For all comparisons, microorganisms were treated in the same way at the same time with devices to minimize the errors related to batch-to-batch differences. To avoid error in Δlog calculations, where the viable bacterium was not detected after a 24-hour growth period, a CFU ml⁻¹ value of 1 (i.e., log1 = 0) was assumed. The SD for Δlog (denoted as S_{LR}) was estimated by using $S_{LR} = [(S_{control}^2/n) + (S_{device}^2/m)]^{1/2}$, where $S_{control}$ and S_{device} are SDs for the log reductions for the control and device treatments, respectively, and *n* and *m* are the number of control and device treatments, respectively.

was treated with harsher conditions ($E_{\rm app}=6$ to 9 V, $\tau_{\rm app}=10$ to 20 min; figs. S15 to S17 and table S5). These studies highlight the roles that the copper export machinery and the reactive oxygen intermediate defense system play in reducing the toxic effects of ROS and copper species in *A. fumigatus* (87). The significant differences in the deactivation efficiency observed among bacteria and fungi underscore the need for optimizing experimental conditions {such as [Cu(II)], $E_{\rm app}$, and $\tau_{\rm app}$ } to achieve high deactivation efficiency with ENM treatments.

The antiviral effectivity of the devices was studied by quantifying the lentiviral transduction in the HEK293T cell line to produce an infrared protein. For these studies, only control and Ag devices were used because ENM devices were found toxic to the mammalian HEK293T cells. The HEK293T cells that were transduced with Agovand Ag_{3V}-treated lentivirion appeared healthy and exhibited confluency similar to healthy nontransduced HEK293T cells. For these experiments, lentivirion were first treated with control or Ag devices ($E_{\rm app}=0,3$, and 6 V, $\tau_{\rm app}=10$ to 20 min). The treated lentivirion were

then transduced into HEK293T cells, which expressed infrared fluorescent protein (iRFP). The fraction change in the emission intensity of the iRFP expressed in the HEK293T cells represents the lentivirion transduction efficiency in the HEK293T cells (88). Thus, a decrease in the emission intensity at 700 nm quantifies a lower iRFP concentration in the cells, which represents successful transduction of the lentivirion. The treatment of the lentivirion with Agov devices exhibited a modest transduction efficiency (n) of 63 \pm 5.7 and 67 \pm 11.5% for $\tau_{\rm app} = 10$ and 20 min, respectively (P < 0.0001 versus control, n = 3; Fig. 3E and Table 2). However, the HEK293T cells transduced with lentivirion treated with Ag_{3V} devices showed a larger reduction in the emission intensity, corresponding to $\eta \approx 86 \pm 6\%$ ($\tau_{app} = 10$ min, n = 3, P < 0.0001 versus control) and $\eta \approx 92 \pm 8\%$ ($\tau_{app} = 20$ min, n = 3, P < 0.0001 versus control) (Fig. 3E and Table 2). These results confirmed that lentivirion were damaged with the Ag_{0V} and Ag_{3V} treatments such that they were either less effective in entering HEK293T cells and/or their effectiveness to transduce HEK293T cells after entering the cells was reduced. We have not investigated which of

Kingdom	Species (CFU ml ⁻¹)	E _{app} (V)	τ _{app} (min)	Viable cell or spore (CFU ml ⁻¹ or spores ml ⁻¹)*	η% [†]	Δlog^{\dagger}	₽ [§]
Bacteria	P. aeruginosa $[C]_0 = 2.8 \times 10^6$	0	5	$5.5 \times 10^5 \pm 1.5 \times 10^5$	80	0.70	ns
	•••	3	5	ND ¹	≈100 ^{**}	6.45	<0.0001
	S. aureus $[C]_0 = 3.0 \times 10^6$	0	5	$3.4 \times 10^5 \pm 1.0 \times 10^5$	88.5	0.94	<0.0001
		3	5	$5.7 \times 10^3 \pm 3.4 \times 10^3$	99.8	2.75	<0.0001
		6	10	ND [¶]	≈100 ^{**}	6.48	<0.0001
	A. baumannii $[C]_{o} = 1.5 \times 10^{6}$	0	5	1.4 × 10 ⁶ ± 4.5 × 10 ⁵	6.3	0.028	<0.0001
		3	5	ND [¶]	≈100 ^{**}	6.18	<0.0001
	SIUC2 and SIUC11 $[C]_0 = 3.1 \times 10^4$	0	5	$4.1 \times 10^2 \pm 3.2 \times 10^2$	98.5	1.9	<0.0001
		3	5	ND ¹	≈100 ^{††,#}	4.5 ^{††} –7.7 [#]	<0.0001
Fungi	C. albicans $C_o = 4.4 \times 10^4$	0	5	$9.5 \times 10^3 \pm 4.0 \times 10^3$	80	0.67	<0.0001
	spores ml ⁻¹	3	5	$3.1 \times 10^3 \pm $	93	1.2	<0.0001

*Viable CFU ml $^{-1}$ or spores ml $^{-1}$ after ENM treatment. $\dagger \eta$ that was estimated using Eq. 2. $\dagger \Delta \log$ that was estimated using Eq. 3. $\S P$ values were calculated using a one-way ANOVA and a Tukey's test for separating means when differences were found (n=3). $\P ND$ denotes viable bacterial cells were not detected in the culture media after a 24-hour growth period. #Studies conducted with a SIUC2-SIUC11 mixture having $[C]_0 = 5 \times 10^7$ CFU ml $^{-1}$, which exhibited $\eta \approx 99.99999\%$ for the ENM_{3V} treatment ($\tau_{app} = 15$ to 20 min; fig. S14). ** $\eta \approx 99.9999\%$ ($\Delta \log > 6$). † $\tau_{app} = 15$ to 20 min; fig. S14).

these two scenarios contributed to a decrease in the iRFP production in the cells. However, these results confirmed that the electrically polarized silver coatings were effective in reducing the transduction of lentivirion in HEK293T cells, which is attributed to generation of 'OH and HOCl by the Ag devices (fig. S18). Although effective in reducing the iRFP concentration, the ROS and RCS concentrations produced by the Ag device treatments were significantly lower than the ROS and RCS concentrations produced with ENM treatments (fig. S18), which were ineffective in deactivating bacterial cells with high efficiency (Fig. 2).

Electron microscopy measurements of physical damage and surface morphology changes in the bacterial cells due to ENM treatment

Changes in the physical dimensions and surface morphology in the bacterial cells subjected to electrically polarized device treatment are expected to provide useful information regarding the deactivation process. We performed electron microscopy measurements on SIUC2 and SIUC11 bacterial cells treated with three types of devices (control, ENM_{0V} , and ENM_{3V}) to gain this information in the bacterial cells. The cells were preserved without substantial distortion by using critical point drying procedure (Supplementary Materials). Figure 4 shows scanning electron microscopy (SEM) images of control (column 1), ENM_{0V}-treated (column 2), and ENM_{3V}-treated (column 3) bacterial cells ($\tau_{app} = 5$ min). Although the untreated SIUC2 and SIUC11 control cells were cylindrical with smooth and uniform surface characteristics, the cells treated with ENM_{0V} showed surficial dot- and filament-like nanoscale structures with width \approx 60 nm and length of a few hundreds of nanometers (n = 14) (Fig. 4, B and E). Although cells were not completely distorted or collapsed, large damage was observed in the cells with ENM_{0V} treatments. These results are consistent with the cell growth studies, which exhibited substantial but not a complete deactivation of the cells treated with ENM_{0V} (Fig. 2 and Table 1). However, ENM_{3V}-treated cells experienced more pronounced damage including significant distortions in shape, volume, and surface texture (Fig. 4, C and F). Furthermore, the ejection and leakage of the internal cellular material are also seen in electron micrographs (dashed oval in Fig. 4C), which is attributed to damage of the bacterial walls and/or membrane. In general, many modes of interactions between bacteria and damaging species can deactivate and kill bacteria, including (i) direct contact of the species with cell walls and/or membranes; (ii) generation of ROS and RCS, which can adversely affect the membranes, nucleic acids (genotoxicity), proteins, and enzymes (proteotoxicity); (iii) impairment of membrane function; and (iv) interference with nutrient assimilation (48, 49). Experiments conducted with devices composed only of Cu(II) and those composed only of Ag did not exhibit deactivation of SIUC2 and SIUC11 with high efficiency (Fig. 2 and fig. S12). This implies that the contribution of metal ions to the microorganism deactivation with ENM treatment is minimum. ROS and RCS are known to kill microorganisms and viruses (89-91) and are attributed to bacteria, fungi, and lentivirus deactivation in this study. However, more studies are needed to elucidate potential biochemical pathways, which led to the membrane damage and pore formation in the membranes, causing leakage of the internal cellular materials.

ROS production using electrically polarized metallic nanoscale coatings

Identification and quantification of the potential chemical species that contributed to the deactivation of microorganisms by the ENM

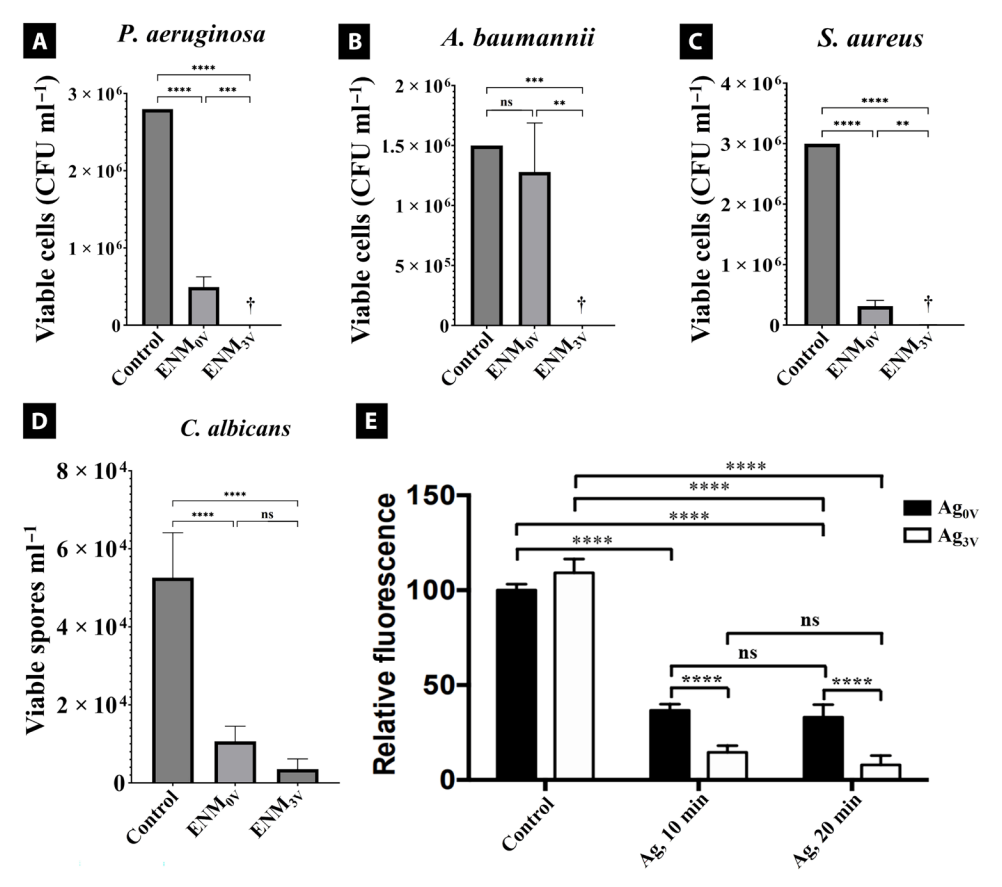


Fig. 3. Viable bacterial cells, fungal spores, and lentivirion deactivation with control and ENM devices. Cell viability of *P. aeruginosa* (**A**), *A. baumannii* (**B**), *S. aureus* (**C**), and spore viability of *C. albicans* (**D**) treated with the control and ENM devices. † denotes that viable *P. aeruginosa*, *A. baumannii*, and *S. aureus* cells were not detected after treatment with ENM_{3V}, ENM_{3V}, and ENM_{6V}, respectively. $[C_o]$ values of *S. aureus*, *A. baumannii*, and *P. aeruginosa* were 3×10^6 , 1.5×10^6 , and 2.8×10^6 CFU ml⁻¹, respectively. $[C_o]$ for the *C. albicans* was 5.5×10^4 spores ml⁻¹. $\tau_{app} = 5$ min was used for the experiments in (A) to (D). (E) Transduction efficiency of the lentivirion treated with control and Ag devices ($E_{app} = 0$ and 3 V) for $\tau_{app} = 10$ and 20 min was estimated using relative fluorescence intensity emission ($\lambda_{em} = 700$ nm) of the iRFP expressed in the HEK293T cells. The emission intensity of HEK293T cells infected with untreated lentivirion was taken as 100 arbitrary units. All the results are presented as the means \pm SD of three independent experiments (n = 3). The SD was not estimated for the treatments when viable cells were not detected after culturing the cells or spores for 24 hours. ns, **, ****, and ***** represent not significant versus control, P = 0.0209 versus control, P = 0.0209 versus control, and P < 0.0001 versus control, respectively. For all comparisons, microorganisms and lentivirus were treated in the same way at the same time with the ENM devices to minimize errors related to batch-to-batch differences.

Virus	$E_{\rm app}\left(V\right)$	$ au_{app}$ (min)	Relative IR emission (%)	η*	SD	₽ [†]
Lentivirus	0	10	37	63	5.7	<0.0001
	3	10	15	85	6.2	< 0.0001
	0	20	33	67	11.5	< 0.0001
	3	20	8	92	8.4	<0.0001

^{*}Transduction efficiency (η) of the lentivirion, which was estimated using the equation $\eta = \left(1 - \frac{I_1}{I_c}\right) \times 100$. I_c and I_f are the IR emission intensities of the HEK293T cells, which were transduced with control-treated lentivirion and Ag-treated lentivirion, respectively. For all the measurements, the background emission was subtracted. †P values that were estimated from three independent experiments using a two-way ANOVA test followed by Bonferroni correction. For these studies, the lentivirion and HEK298T concentrations were 8×10^6 titer unit ml⁻¹ and 10^4 cells ml⁻¹, respectively.

treatment are important. This will help improve understanding of the deactivation processes involved in the treatment. The changes in temperature and pH of the aqueous solutions treated with ENM devices ($E_{\rm app}=3$ to 6 V, $\tau_{\rm app}=5$ to 15 min) were <2°C and <1 pH unit, respectively (figs. S19 and S20). Furthermore, because Cu(II)-containing devices without silver coatings were not effective in the deactivation

of the microbes investigated in the studies (Fig. 2 and fig. S12), we therefore rule out any large contributions from factors such as temperature, pH, and cupric ions to the observed deactivation of the microorganisms and lentivirus with the ENM treatment. We provide below spectroscopic quantification of ROS and RCS, which are implicated in the antimicrobial and antiviral properties of ENM devices.

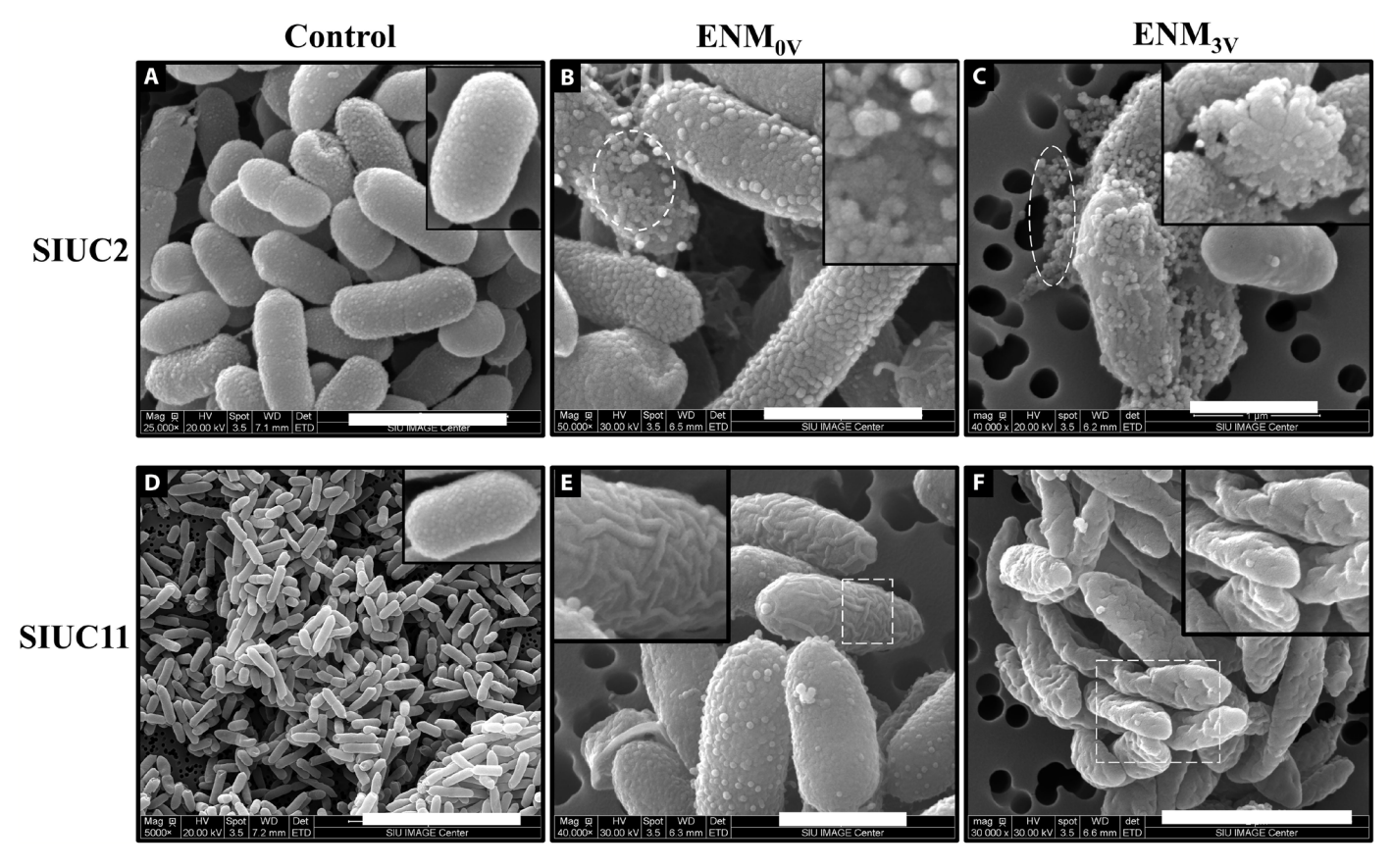


Fig. 4. SEM measurements of control, ENM_{0V}-treated, and ENM_{3V}-treated SIUC2 and SIUC11 bacteria. Column 1: SEM images of (**A**) untreated control SIUC2 and (**D**) SIUC11 cells. The length and width of the SIUC2 cells were \approx 1192 \pm 342 and 667 \pm 45 nm (n = 50), respectively, and the SIUC11 cells exhibited the length and width of \approx 1708 \pm 417 and 623 \pm 33 nm, respectively (n = 50). Column 2: SEM images of the ENM_{0V}-treated (**B**) SIUC2 and (**E**) SIUC11 cells. Column 3: SEM images of the ENM_{3V}-treated (**C**) SIUC2 and (**F**) SIUC11 cells. The insets in (E) and (F) represent magnified micrographs of the white dashed squares in (E) and (F), respectively, whereas the insets in (B) and (C) show magnified micrographs of the white dashed ovals in (B) and (C), respectively. ENM_{0V}- and ENM_{3V}-treated cells exhibited their large physical deformations, and leakage of the intracellular material is also observed. Scale bars, 1 μm [(B), (C), and (E)], 2 μm [(A) and (F)], and 10 μm (D).

Cu(I) generation by ENM devices

The in situ production of Cu(I) is key to the generation of micromolar concentrations of ROS and ROS observed in ENM-treated solutions. Therefore, Cu(I), H₂O₂, OH, and HOCl were spectroscopically quantified. The concentration of Cu(I) (denoted as [Cu(I)]) was measured in the ENM_{0V}- and ENM_{3V}-treated solutions by using the bathocuproine disulfonate (BCS) complexation method. BCS is a highly selective Cu(I) sensor, which provides accurate estimation of [Cu(I)] in aqueous solutions (92, 93). All the experiments were performed in the dark to avoid interference from photochemically activated reactions (pH = 7, temperature = 22°C). The linear Cu(I) production rates of 0.76 and 0.34 μ M cm⁻² min⁻¹ for $\tau_{app} = 0$ to 10 min were observed for ENM_{3V} and ENM_{0V} treatments, respectively (Fig. 5). Furthermore, more than twice [Cu(I)] ($\approx 15 \,\mu\text{M cm}^{-2}$) was produced in the solutions treated with ENM_{3V} ($\tau_{app} = 2$ hours) than that was produced with ENM_{0V} (\approx 6.5 μ M cm⁻²) (Fig. 5, A to C). Furthermore, a significantly smaller initial [Cu(I)] production rate and a much shorter time to attain a pseudo-steady state was observed for ENM_{0V} than that for the ENM_{3V} treatment. For example, the Cu(I) generation was plateaued at $\tau_{app} = 45 \mbox{ min}$ for the ENM $_{0V}$ treated solutions, whereas a pseudo-steady-state Cu(I) concentration of ([Cu(I)]_{ss}) $\approx 23 \,\mu\text{M cm}^{-2}$ was achieved at $\tau_{app} = 1440 \,\text{min}$

(1 day) for the ENM $_{3V}$ treatment. Therefore, $[Cu(I)]_{ss} \approx 3$ and 11% of the initial Cu(II) concentration were generated in the solutions treated with ENM $_{0V}$ and ENM $_{3V}$, respectively. These experiments suggested that a sustainable long-term generation of [Cu(I)] was achieved with ENM $_{3V}$ treatments, which may provide effective antimicrobial and antiviral properties to ENM devices for an extended period of time.

 Ag_{0V} and Ag_{3V} devices also produced [Cu(I)] when these devices were placed in 240 nM Cu(II) aqueous solutions. The [Cu(I)] for the Ag_{3V} treatments was, however, about 3 times and >27 times lower than that for ENM_{0V} and ENM_{3V} treatments ($\tau_{app}=90$ min), respectively (Fig. 5C). This indicates a more efficient Cu(II) reduction by both ENM_{0V} and ENM_{3V} devices. One of the possible reasons for the larger [Cu(I)] and its production rate in the ENM-treated solutions is the intimate contact of Cu(II) with conductive coating in ENM devices, which is likely to facilitate Cu(II) reduction rate. However, diffusion of the hydrated cupric ions to the silver electrodes is needed for Cu(I) production in Ag_{0V} and Ag_{3V} devices, which is a slower process. Furthermore, aggregation of Cu(II) on the ENM surfaces leads to considerably larger Cu(II) local concentration, potentially contributing to an enhance Cu(II) reduction rate for the ENM treatments.

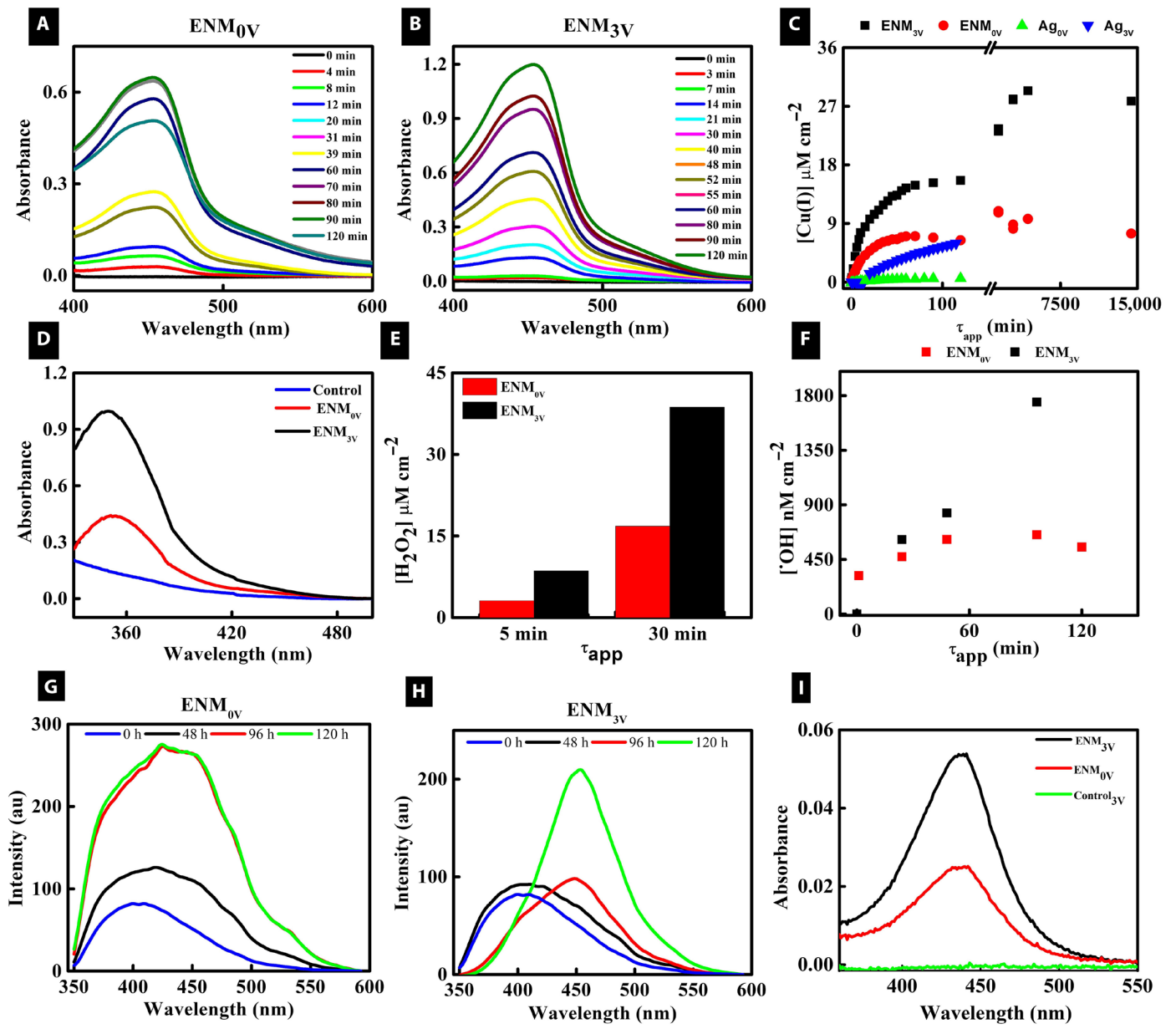


Fig. 5. Spectroscopic quantification of Cu(I), ROS, and RCS generated in the aqueous solution treated with ENM_{0V} and ENM_{3V} devices. Electronic absorbance spectra of Cu(I)-BCS complex for (**A**) ENM_{0V} and (**B**) ENM_{3V} treatments for $\tau_{app} = 0$ to 120 min. (**C**) [Cu(I)]- τ_{app} dependence for ENM_{0V} (red), ENM_{3V} (black), Ag_{0V} (green), and Ag_{3V} (blue) devices. (**D**) Ultraviolet-visible (UV-Vis) spectra for the [H₂O₂] estimation using the I³⁻ method for ENM_{0V} (red), ENM_{3V} (black), and the control surface (blue) treated for $\tau_{app} = 30$ min. (**E**) [H₂O₂]- τ_{app} dependence for the aqueous solutions treated with ENM_{0V} (red) and ENM_{3V} (black) devices for $\tau_{app} = 5$ and 30 min, respectively. (**F**) The [*OH]- τ_{app} dependence for ENM_{0V}-treated (red) and ENM_{3V}-treated (black) solutions was estimated using the NDA assay. The emission spectra of a 0.1 mM coumarin solution treated with ENM_{0V} (**G**) and ENM_{3V} (**H**) devices for $\tau_{app} = 0$ hour (blue), 48 hours (black), 96 hours (red), and 120 hours (green). The device size for the experiments performed in (G) and (H) was 16 cm². (I) UV-Vis spectra of o-tolidine containing an aqueous solution treated with control (green), ENM_{0V} (red), and ENM_{3V} (black) devices. $\tau_{app} = 60$ min, device area = 1 cm², and [Cl⁻] = 0.30 mM were used for (I). All the experiments were performed in the dark (pH = 7 and temperature = 22°C). For data in (A) to (C), [BCS] = 250 μM, ENM device area = 0.5 to 2 cm², and volume of the solution = 2 ml. For Ag device experiments in (C), [Cu(II)] = 240 nM was used.

Micromolar H₂O₂ was produced by ENM treatment

The $[H_2O_2]$ in the ENM-treated solutions was spectroscopically estimated using the I^{3-} method (94). For 5-min treatment, the ENM $_{0V}$ and ENM $_{3V}$ devices yielded $[H_2O_2]\approx 3$ and 8.6 μM cm $^{-2}$, respectively, whereas $[H_2O_2]\approx 17$ and 39 μM cm $^{-2}$ for ENM $_{0V}$ and ENM $_{3V}$, respectively, were formed for $\tau_{app}=30$ min treatments (Fig. 5, D and E). These results agree with the [Cu(I)]- τ_{app} trend for ENM $_{0V}$ and

 ENM_{3V} devices, where the [Cu(I)] production rate for ENM_{3V} devices was more than twice that for the ENM_{0V} devices for over 90-min duration (Fig. 5C). The control experiments with unfunctionalized surfaces did not exhibit production of H_2O_2 under the same experimental conditions (Fig. 5D).

 H_2O_2 was produced in the aqueous ENM-treated solutions by a two-step reaction mechanism (71, 73). The first step involves

Cu(I)-mediated oxygen reduction to superoxide (Eqs. 4 and 5), which is followed by a second one-electron reduction through either superoxide disproportionation reaction (Eq. 7) or Cu(I)-mediated $O_2^{\bullet,\bullet}$ reduction (Eq. 8). The detection of $[O_2^{\bullet,\bullet}]$ by the ferric cytochrome c to ferrous cytochrome c reduction assay was not successful in our experiments. We estimate a pseudo-steady-state $[O_2^{\bullet,\bullet}]_{ss}$ in the picomolar range (Supplementary Materials), which is two to three orders of magnitude smaller than the lowest concentration of cytochrome c that can be measured using absorption spectroscopy. This low $[O_2^{\bullet,\bullet}]$ is a result of the rapid consumption of $O_2^{\bullet,\bullet}$ through multiple deactivation pathways (Eqs. 7, 8, 10, and 12), where the reaction of $O_2^{\bullet,\bullet}$ with species, such as Cu(I), Cu(II), $O_2^{\bullet,\bullet}$, and Ag NPs present in solution, is fast (rate constants of ~10⁸ to 10^{10} M $^{-1}$ s $^{-1}$; Fig. 6). As discussed earlier, another possibility of the H_2O_2 production is through a single two-electron O_2 reduction process (75, 77, 78).

*OH and HOCI production in ENM-treated aqueous solutions

The *OH in aqueous solutions treated with ENM_{0V} and ENM_{3V} devices was spectroscopically quantified using two molecular probes: p-nitrosodimethylaniline (NDA) (95) and coumarin (96)—both probes are selective for the *OH detection. Figure 5F shows [*OH]- τ_{app} dependence for ENM_{0V} and ENM_{3V} using the NDA assay. The [*OH] for the ENM_{3V} was 900 nM cm⁻² for τ_{app} = 45 min treatment, which was found to increase linearly for τ_{app} ~ 100 min. The [*OH] for the ENM_{3V} devices was >4 times larger than that was observed for the ENM_{0V}-treated solution (τ_{app} = 100 min) (Fig. 5F and fig. S21). These results agree with both [Cu(I)]- τ_{app} and [H₂O₂]- τ_{app} trends and are also consistent with the overall *OH production mechanism, where H₂O₂ and Cu(I) are involved in the *OH generation in the solutions.

The presence of *OH in the solutions treated with ENM_{0V} and ENM_{3V} devices was also confirmed by the appearance of a strong 7-hydroxycoumarin (7HC) emission peak centered at 456 nm. 7HC is known to form by oxidative attack of *OH on coumarin (96). Unlike a relatively sharp emission band for pure 7HC centered at $\lambda_{em}\approx 454$ nm for the ENM_{3V} solutions ($\tau_{app}\approx 96$ hours), the emission spectrum for the ENM_{0V} devices exhibited a much broader emission band with full width at half maximum (FWHM) ≈ 130 nm (Fig. 5, G and H). A significant increase in the FWHM of the emission spectrum of ENM_{0V}-treated solution suggested the presence of both coumarin and 7HC species in the solutions, whereas it appears that all the coumarin was converted into 7HC. These results confirmed that much larger [*OH] were produced with ENM_{3V} treatment than ENM_{0V} treatment. In addition, the experiments with control surfaces did not exhibit a 7HC emission peak, which is not unexpected.

Using a calibration curve (fig. S22C), $[{}^{\bullet}OH] \approx 272 \text{ pM cm}^{-2}$ ($\tau_{app} = 96 \text{ hours}$) to 575 pM cm⁻² ($\tau_{app} = 120 \text{ hours}$) were obtained for the ENM_{3V}-treated solutions. Although the $[{}^{\bullet}OH]$ for short τ_{app} was not estimated in the 7HC assay because of the large overlap between coumarin and 7HC peaks, the NDA assay clearly indicated ${}^{\bullet}OH$ production in the ENM solutions for short $\tau_{app} < 120 \text{ min treatments}$. The $[{}^{\bullet}OH]$ estimated from the 7HC assay was substantially lower than the $[{}^{\bullet}OH]$ estimated using the NDA assay (Fig. 5F). This large difference in the $[{}^{\bullet}OH]$ estimated using these assays is attributed to quenching of 7HC emission by various reactive species, including superoxide, H_2O_2 , RCS, and metal ions, present in the solutions (fig. S22). Therefore, we emphasize that the $[{}^{\bullet}OH]$ estimated using the 7HC emission method lowers its expected concentration in the solution.

The presence of HOCl was confirmed in the aqueous solutions that were treated with the ENM devices. HOCl is known to form from $\rm H_2O_2$ in the presence of Cl $^-$ and copper ions (70). In the presence of o-tolidine, the ENM $_{\rm 0V}$ - and ENM $_{\rm 3V}$ -treated solutions turned yellow due to the formation of holoquinone (97), confirming the presence of HOCl in the solution (Fig. 5I and tables S6 and S7). Although the holoquinone absorption peak at 437 nm was absent for solutions treated with control devices, under the same experimental conditions, more than twice HOCl (3.6 μM cm $^{-2}$) was produced in the solutions treated with ENM $_{\rm 3V}$ for $\tau_{\rm app}$ = 60 min than that was observed with the ENM $_{\rm 0V}$ treatment (1.7 μM cm $^{-2}$) (Fig. 5I, fig. S23, and tables S6 and S7).

Lastly, both the ENM $_{0V}$ and ENM $_{3V}$ devices also exhibited fast oxidation of ascorbic acid (a known antioxidant). The ascorbic acid oxidation rates were 1.2 and 0.8 μ M cm $^{-2}$ s $^{-1}$ for ENM $_{3V}$ and ENM $_{0V}$ treatments, respectively (figs. S24 and S25). Collectively, the spectroscopic results confirmed that the electric polarization of the metallic Cu(II)-Ag nanoscale coatings produced highly reactive ROS and RCS in the solutions. Additionally, although the ENM $_{0V}$ devices produced lower ROS and RCS concentrations than those observed for the ENM $_{3V}$ treatments, they still exhibited modest antimicrobial properties, implying that ENM devices can be used in the active mode. That is, the antimicrobial efficacy of ENM devices can be modulated with applied electric potential. Furthermore, ENM devices retained antimicrobial effectivity even after the applied electric potential was reset to 0 V although with a lower deactivation efficiency than ENM $_{3V}$ devices.

DISCUSSION

Because of recent outbreaks of highly infectious diseases and the emergence of antimicrobial bacteria, new materials and devices that deactivate and kill a wide range of microorganisms and viruses are urgently needed. In this study, we demonstrate effective deactivation of broad-spectrum microorganisms and lentivirus by implementing electrical polarization of nanoscale copper-silver coatings. ENM devices were powered by an external low-power battery and consume power in the milliwatt regime. Conventional alkaline batteries or solar cells powered ENM devices for many hours without any observable decrease in performance. We explore below three important points that are crucial to understanding of the various processes involved in the ENM treatments that yielded broad-spectrum antimicrobial properties to the ENM devices: (i) the potential pathways and reactions for the production of ROS and RCS; (ii) discussion concerning physical and chemical processes, which are potentially involved in the generation of Cu(I), H₂O₂, OH, and HOCl at distances much farther away from the ENM devices; and (iii) discussion concerning an observed long-term sustainable concentration of Cu(I) and OH in the ENM-containing solutions.

Mechanisms and pathways for the production of ROS and RCS in solutions treated with the ENM devices

Figure 6A shows two major parts that depict various major redox pathways for Cu(0/I/II) cycling and generation of ROS and RCS in solutions treated with the ENM devices. This figure is not comprehensive, but it is intended to provide major potential reactions relevant to the present studies. The bottom square emphasizes the production of ROS and RCS mediated by the copper redox chemistry, whereas the top triangle depicts reactions involving cycling of

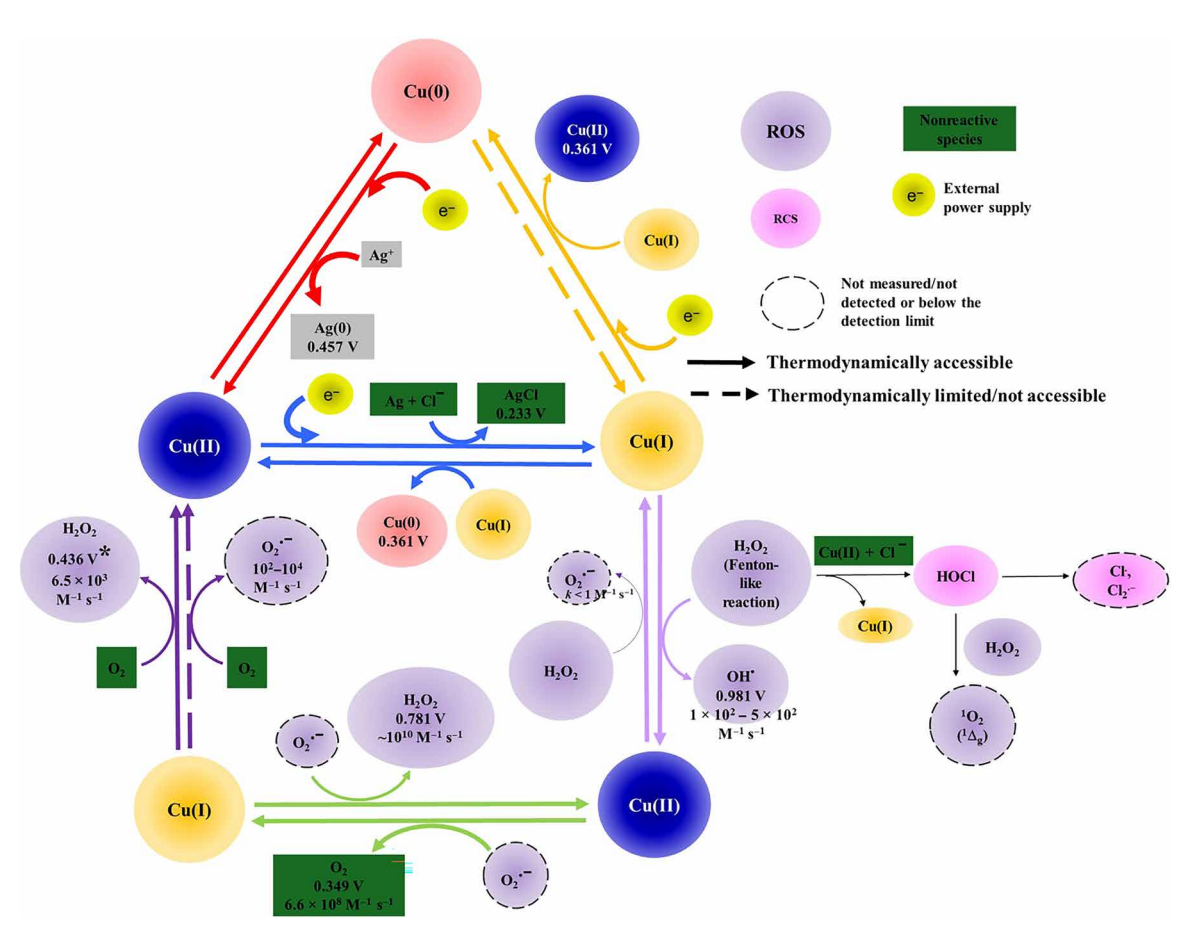


Fig. 6. Redox reaction pathways that generated ROS and RCS in ENM-treated solutions. The figure contains two parts: triangle (top) and square (bottom) redox cycles. The top triangle provides Cu(0/I/II) redox reactions occurring in the solutions treated with ENM devices. The bottom square provides various possible reactions that generate ROS and RCS in the system. The size of the circle represents the expected/measured concentration of the species. Purple-colored (ROS) and pink-colored (RCS) species are reactive to cells, whereas gray-colored rectangles are less reactive/nontoxic to cells. For some reactions, half-cell reduction potential (in volts) and second-order rate constants (in M^{-1} s⁻¹) are also provided. The dashed circles in the rectangular part represent species that were either not detected or formed at concentrations, which we were not able to detect. The solid and dashed arrows represent thermodynamically accessible and thermodynamically inaccessible/less accessible reactions, respectively. The external power is represented by a yellow circle with e^- . H_2O_2 can be generated by two successive one-electron reduction mechanisms or a single two-electron O_2 reduction. The later mechanism is denoted by *. Some reactions depicted in the figure can occur through multiple pathways. Not all possible reaction pathways are shown in the figure.

Cu(0/I/II) species. In some cases, standard reduction potentials and rate constants were also provided in Fig. 6. The rate constants of some reactions in Fig. 6 may depend on the experimental conditions; however, they provide useful information regarding the kinetics of the reactions.

Reactions pathways for $O_2^{\bullet-}$ and H_2O_2 production and consumption

The first step in the production of ROS and RCS is the Cu(I)-mediated one-electron reduction of O_2 to $O_2^{\bullet-}$ (Eqs. 4 to 6), which is followed by a second one-electron reduction to generate H_2O_2 (Eq. 8) (71–75). Thus, two Cu(I) species are involved in two successive one-electron reduction reactions for H_2O_2 production. A two-electron reduction of O_2 to H_2O_2 reduction reaction using two Cu(I) species is also proposed in the literature (Eq. 9). As mentioned earlier, this reaction is thermodynamically accessible ($E_0 = 0.436$ V) (79) but has a low rate constant ($k_{5'} = 6.5 \times 10^3 \, \text{M}^{-1} \, \text{s}^{-1}$) (77). Furthermore, two closely located Cu(I) species are necessary for a single two-electron O_2 reduction to H_2O_2 . With [Cu(I)] $\approx 30 \, \mu \text{M} \, \text{cm}^{-2}$,

the probability of availability of two Cu(I) in close proximity in the bulk solution for the two-electron reduction reaction is expected to be small, although this reaction is feasible in the Cu(II) aggregated state on the solid surfaces. In any case, Cu(I) plays a crucial role in the generation of H_2O_2 in both the mechanisms. However, because of a lack of clarity, we consider that both the reaction mechanisms can be operable in the production of H_2O_2 in the ENM treatment (Fig. 6).

In general, the oxygen reduction by Cu(I) to $O_2^{\bullet-}$ can occur through three major reaction pathways at circumneutral pH (Eqs. 4 to 6; purple arrowed reaction in Fig. 6) (73), where k_i are second-order rate constants (71, 73, 98). Equations 4 and 5 are available in the present studies (dark purple arrow, Fig. 6); the third reaction (Eq. 6), however, contributes negligibly to the production of $O_2^{\bullet-}$ in the present studies

$$Cu^{+} + O_{2} \rightarrow Cu(II) + O_{2}^{\bullet -}$$

 $k_{1} = 3.1 \times 10^{4} \text{ M}^{-1} \text{ s}^{-1}$ (4)

CuClOH⁻ +O₂
$$\rightarrow$$
 Cu(II) +O₂•-
 $k_2 = 3.1 \times 10^2 \text{ M}^{-1} \text{ s}^{-1}$ (5)

$$CuCO_3^- + O_2 \rightarrow Cu(II) + O_2^{\bullet-}$$

 $k_3 = 1.0 \times 10^4 \text{ M}^{-1} \text{ s}^{-1}$ (6)

The rate constants (k) for Eqs. 4 to 6 depend on [Cl⁻] and other experimental conditions. The reported k values for Eqs. 4 to 6 are for experimental conditions containing [Cl⁻] = 0.2 to 0.7 M, pH = 6.6 to 8.0, and ionic strength = 0.7 M (73, 99). In general, the reduction of O₂ with copper species is usually expressed in terms of total Cu(I) and Cu(II) concentrations rather than explicit individual ionic species. This is due to Cu(I) stabilization by ligands (such as Cl⁻) in the solution. The relative concentrations of Cu(I)-Cl complexes, such as CuCl(s), CuCl₂⁻, and CuCl₃²⁻, depends on [Cl⁻] (73).

CuCl(s), CuCl₂⁻, and CuCl₃²⁻, depends on [Cl⁻] (73). The consumption of $O_2^{\bullet-}$ occurs through multiple pathways, as depicted in Eqs. 7 to 12 and 16. The $O_2^{\bullet-}$ disproportionation reaction (Eq. 7) and Cu(I)-mediated $O_2^{\bullet-}$ reduction (Eq. 8) are two potential pathways for H_2O_2 generation in the ENM-treated solutions (one-electron reduction mechanism). Because $k_4 \ [O_2^{\bullet-}]^2 \ll k_5 \ [Cu(I)] \ [O_2^{\bullet-}]$, the $O_2^{\bullet-}$ disproportionation reaction appears play a minor role in H_2O_2 production, and the predominant contributor to observed for H_2O_2 is the Cu(I)-mediated $O_2^{\bullet-}$ reduction reaction (green arrow, Fig. 6).

Recently, Waite's group reported that Ag NPs can also react with $O_2^{\bullet-}$ with diffusion-limited rate constant $(k_9 \approx 1 \times 10^{10} \text{ M}^{-1} \text{ s}^{-1})$. Thus, Ag NPs can provide another potential draining pathway for O₂ consumption (100). We used dynamic light scattering to investigate if NPs were generated in the ENM-treated solutions. NPs were not detected in the ENM_{3V}-treated solutions for $\tau_{app} = 5$ hours. However, the solutions treated with ENM_{3V} for $\tau_{app} = 24$ hours exhibited NPs of radius ≈ 100 nm (fig. S26). Although the exact chemical nature of the NPs is not conclusively known at this time, both the silver NPs and copper-containing NPs are known to react with O2 (100–102). Therefore, the contribution of reactions between O_2^{\bullet} and Ag NPs can be neglected in the overall reaction scheme for short τ_{app} ENM treatments. However, given fast kinetics with diffusionlimited rate constants, these reactions may become important to consider for the long ENM treatments. In summary, the interplay of multiple reactions (Eqs. 1, 2, 8, 10, and 12) dictates the generation of H_2O_2 in the ENM-treated solutions.

Reaction pathways for *OH and HOCI generation and consumption

Both $O_2^{\bullet-}$ and H_2O_2 are substantially less reactive to cellular and lentivirus components than 'OH. 'OH is the most reactive ROS generated in cellular systems (50, 103). 'OH is known to react with cellular species with a diffusion-limited reaction rate constant of 10^9 to $10^{10} \, \mathrm{M}^{-1} \, \mathrm{s}^{-1}$ (50). In ENM-treated solutions, 'OH was produced by a Fenton-like reaction between Cu(I) and H_2O_2 (light purple arrow, Fig. 6). The reaction between Cu(II) and H_2O_2 for 'OH production is extremely slow [Eq. 14, $k_{13} < 1 \, \mathrm{M}^{-1} \, \mathrm{s}^{-1}$ (98)]. Therefore, the contribution of Eq. 14 to the overall 'OH production is likely to be small (Fig. 6).

Unexpectedly, the 7HC emission experiments confirmed that OH was produced for $\tau_{app} > 96$ hours in the ENM-treated solutions. Because the OH production requires both H_2O_2 and Cu(I), it follows that these two species were available in the solutions for an extended period of time. H_2O_2 is quite stable in the aqueous solutions having a lifetime

of ~1 to 2 days (104) and with a diffusion distance $(d_{H2O2}) \approx \text{up to}$ millimeters in the aqueous solutions (50). Furthermore, although the lifetime of Cu(I) is on the order of minutes, the experiments confirmed the generation of Cu(I) in the ENM-treated solutions for many hours (Fig. 5C). Thus, the availability of both the H₂O₂ and Cu(I) in the solutions over extended periods supports the 'OH production in the solutions treated with ENM devices for a long period of time. Similarly, ENM treatments also generated micromolar HOCl in the solutions (Fig. 5I). HOCl is known to form through a reaction of H_2O_2 with Cl^- in the presence of Cu(II) (70), where all the species are stable under the aqueous conditions. This reaction also reduces Cu(II) to Cu(I), providing another source of Cu(I) in the bulk solution (Eq. 17). Lastly, although the detection of other ROS (such as ${}^{1}O_{2}$) (105), RCS (Cl and Cl , and reactive nitrogen species (such as nitric oxide and peroxynitrite) was not attempted, their presence in the ENM-treated solution cannot be not ruled out (Fig. 6).

Figure 7 represents the overall proposed mechanism for the production of ROS and RCS in the ENM-treated solutions. First, Cu(II) in a water droplet (blue hemisphere) was reduced to Cu(I) using external battery sources and the Walden reductor (Fig. 7, 1). H₂O₂ was produced through either two one-electron reduction reactions (Fig. 7, 2 to 3 to 4) or a single two-electron reduction reaction (Fig. 7, 2 and 3'). Although *OH was produced by the H₂O₂ decomposition catalyzed by Cu(I) (Fig. 7, 5), HOCl was generated by a reaction between H₂O₂ and Cl⁻ catalyzed by Cu(II) (Fig. 7, 6). These reactions were repeated in the solution producing ROS and RCS for an extended period, where recurring Cu(0/I/II) redox cycles played a crucial role.

Possible reactions involving consumption of $O_2^{\bullet-}$ and production of H_2O_2 (Fig. 6)

$$O_2^{\bullet -} + O_2^{\bullet -} + 2H^+ \to H_2O_2 + O_2$$

 $k_2 = 8.3 \times 10^5 \text{ M}^{-1} \text{ s}^{-1} \text{ (pH} = 7)$
(7)

$$Cu(I) + O_2^{\bullet -} + 2H^+ \rightarrow Cu(II) + H_2O_2$$

 $k_5 = 2 \times 10^9 \text{ M}^{-1} \text{ s}^{-1}$ (8)

$$2Cu(I) + O_2 + 2H^+ \to 2Cu(II) + H_2O_2$$

$$k_{5'} = 6.5 \times 10^3 \text{ M}^{-1} \text{ s}^{-1} \text{ a}$$
(9)

Cu(II) + O₂
$$\rightarrow$$
 Cu(I) + O₂
 $k_6 = 6.6 \times 10^8 \text{ M}^{-1} \text{ s}^{-1}$ (10)

$$Ag^{+} + O_{2}^{\bullet -} \rightarrow Ag NP + O_{2}$$

 $k_{8} = 64.5 (\pm 16.3)$ (11)

Ag NP+O₂•
$$\rightarrow$$
 Ag NP*+O₂

$$k_0 = 1 \times 10^{10} \text{ M}^{-1} \text{ s}^{-1}$$
(12)

The potential reactions involving consumption of H_2O_2 and generation of ${}^{\bullet}OH$ (Fig. 6)

$$Cu(I) + H_2O_2 \rightarrow Cu(II) + {}^{\bullet}OH + OH^-$$

 $k_{10} = 1.0 \times 10^2 \text{ M}^{-1} \text{ s}^{-1} \text{ to } 5 \times 10^2 \text{ M}^{-1} \text{ s}^{-1}$ (13)

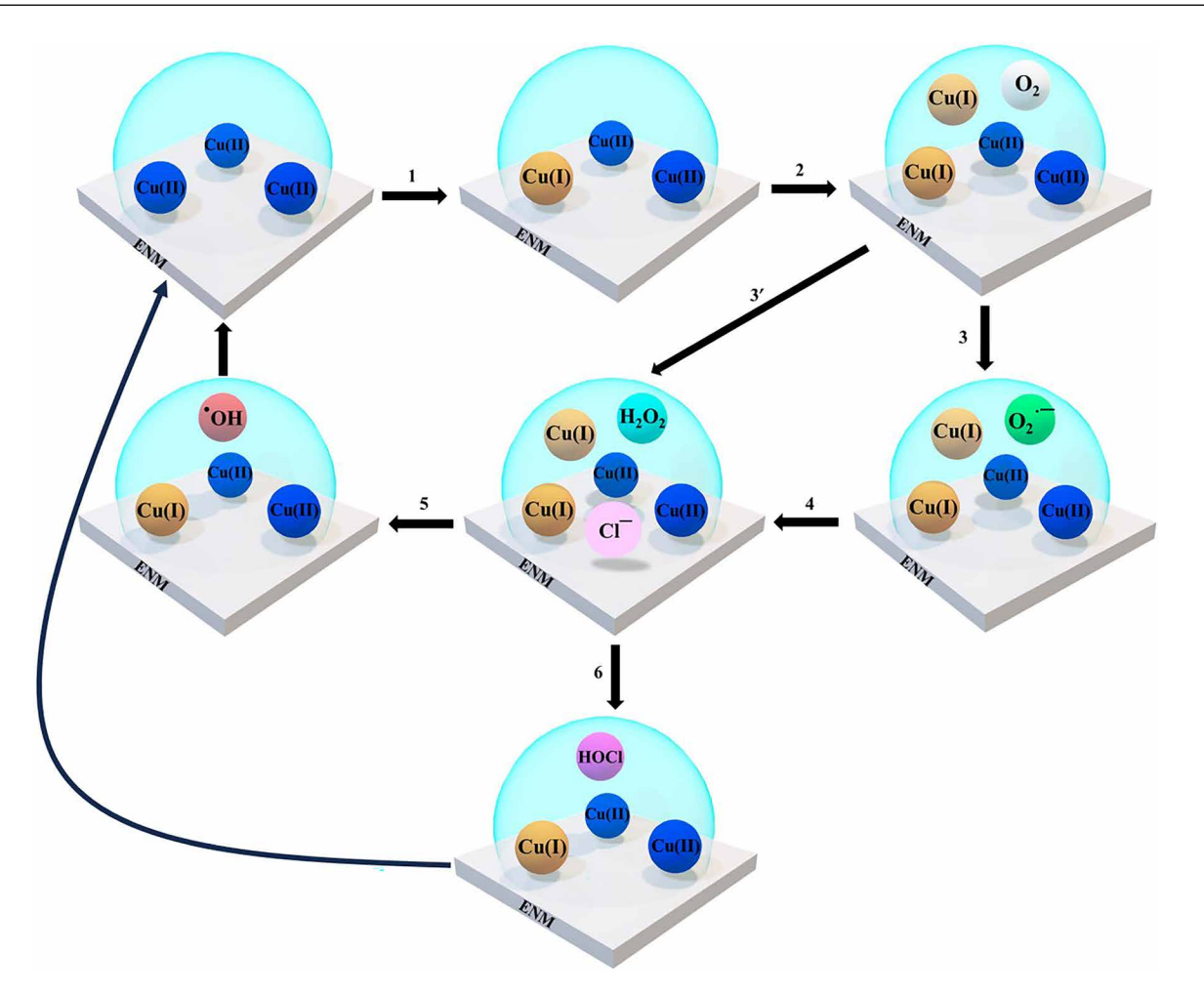


Fig. 7. Schematic of the proposed mechanism of ROS and RCS formation in the bulk solution with ENM treatment. The large hemispheres represent aqueous droplets ranging from many hundreds of micrometers to centimeter in dimension. (1) Electrochemical and electrically induced reduction of Cu(II) (blue sphere) to Cu(I) (yellow sphere) on the ENM electrode. (2) O₂ diffuses to the ENM-water interface, whereas Cu(I) can diffuse away from the ENM-water interface. (3) O₂ is reduced to O₂⁻⁻ (green sphere). (4) Cu(I)-mediated reduction of O₂⁻⁻ produces H₂O₂ (light blue sphere) in the bulk solution. (3') Two-electron O₂ reduction produces H₂O₂ using two Cu(I) species. (5) A Fenton-like reaction between H₂O₂ and Cu(I) produces 'OH (red sphere). (6) Reaction of H₂O₂ in the presence of Cu(II) and Cl⁻ produces HOCI (purple sphere). 'OH and HOCI can react with microorganisms and lentivirus, killing or deactivating them. The recycling of Cu(II) to Cu(I) reduction through electrical polarization mechanism allows the generation of ROS and RCS for an extended period of time in the solution. Hypothetical scale bars provide the dimensions of the water droplets. lons, radicals, and other molecular species are not drawn to the scale.

$$Cu(II) + H_2O_2 \rightarrow Cu(I) + O_2^{\bullet -}$$

 $k_{11} < 1 \text{ M}^{-1} \text{ s}^{-1}$

Ag NP+
$$H_2O_2 \rightarrow Products$$

 $k_{12} = 2.7 \times 10^2 \text{ M}^{-1} \text{ s}^{-1} \text{ (size dependent)}$

$$O_2^{\bullet -} + H^+ + H_2O_2 \rightarrow O_2 + {}^{\bullet}OH + OH^-$$

 k_{13} negligible for practical purposes

$$H_2O_2 + Cl^- + Cu(II) \rightarrow HOCl + Cu(I) + H_2O$$

 k_{14} (value was not given)

- Here, superscript "a" in Eq. 9 represents a two-electron reduction reaction between Cu(I)(bipydyl)₂ and O₂ (77). Ag NP* denotes products of O₂ "/Ag NP reaction (100). k₁₀ is reported for [Cl⁻] between 0.1 and 0.6 M, pH = 8, and T = 298 K. k_i for Eqs. 8 to 17 may vary depending on experimental conditions. Equation 16 is a part of Haber-Weiss cycle, but it contributes insignificantly to
- is a part of Haber-Weiss cycle, but it contributes insignificantly to OH production, in the absence of catalyst, due to slow reaction kinetics.

(16) Production of Cu(I), OH, and HOCI at distances farther away from ENM devices

*OH is the most reactive and damaging known ROS produced in biological systems (103). The reaction between *OH and cellular species occurs with a diffusion-limited rate constant of $\sim 1 \times 10^{10} \,\mathrm{M}^{-1} \,\mathrm{s}^{-1}$. The *OH diffusion distance (d_{OH}) is, however, extremely short (<10 nm)

(17) OH diffusion distance (d_{OH}) is, however, extremely short (<10 nm) (106). Therefore, a reaction between OH and cellular species is expected

to occur within a limited spatial volume of $<10^3$ nm³, which is ~ 5 to 7 orders of magnitude smaller than a typical cell volume. Similarly, HOCl is also a potent oxidant, which damages and kills cells and has a diffusion distance of HOCl ($d_{\rm HOCl}$)—on the order of a micrometer (smaller than a typical cell) (50). The observed high effectiveness for deactivating microorganisms and lentivirion present within ENM-treated droplets of volume $\sim 0.1~{\rm cm}^3$ suggests that microorganisms and lentivirion were present within the diffusion distances of OH and HOCl. This also agrees with experiments that confirmed the presence of Cu(I), OH, and HOCl in ENM-treated bulk solutions (Fig. 5).

Both 'OH and HOCl were produced by the reactions that involved H₂O₂ and copper species. We therefore consider diffusion distances and the availability of O₂ and Cu(I) in the bulk solution to explain the generation and availability of ROS and RCS in bulk solutions. The half-life of Cu(I) $(t_{1/2,Cu})$ ranges from less than a minute (at pH ~ 7) to many minutes, depending on [Cl⁻] and the pH of the solution (73, 107). The estimated diffusion distance of Cu(I) $(d_{\text{Cu}} \approx \sqrt{2D_{\text{Cu}}t_{1/2,\text{Cu}}})$ is thus 309 µm to 780 µm. Here, the $t_{1/2,Cu}$ and diffusion coefficient (D_{Cu}) for Cu(I) were taken as 30 s to 3 min and 1.6×10^{-5} cm² s⁻¹ (108), respectively. Similarly, with the reported half-lifetime of O_2 $(t_{1/2,O_2}) \sim 120 \text{ s}$ (109) and $D_{O_2} = 7.6 \times 10^{-8} \text{ cm}^2 \text{ s}^{-1}$ (pH = 5.4) (110), the estimated diffusion distance $(d_{O_{\bullet}})$ for $O_{2}^{\bullet-}$ is ~42 µm. Thus, based on these simple estimations, both $Cu(\hat{I})$ and $O_2^{\bullet -}$ can diffuse many tens of micrometers, contributing to the production of ROS and RCS in the bulk solution. d_{Cu} and $d_{O_{\bullet}^{*-}}$ in our experiments, however, are likely to be smaller than the estimated diffusion distance values because of the availability of multiple deactivation reaction pathways available in the solution (Eqs. 7 to 10 and 13). HOCl, on the other hand, was produced by a reaction between two stable species, H₂O₂ and Cu(II), contributing to its generation at distances farther away from the ENM devices (Eq. 17). This reaction is also a source of Cu(I) in the bulk solution, aiding in ROS generation in the bulk solution. Lastly, another mechanism that can generate Cu(I) in the bulk solution is a reaction between O₂*- and Cu(II) (Eq. 10) (71), which has a relatively fast kinetics ($k_6 = 6.6 \times 10^8 \,\mathrm{M}^{-1} \,\mathrm{s}^{-1}$). In any case, these simple estimations suggest that ROS and RCS can be generated by diffusion of the reactive species, allowing deactivation of microorganisms and lentivirion in the bulk solution.

Although *OH was detected in the ENM-treated bulk solutions, studies are needed to estimate the local *OH and HOCl concentrations inside or close to bacterial cells, fungal spores, and lentivirion. These studies may also shed light on relative contributions of ROS and RCS to the observed deactivation of the microorganisms and lentivirus. Moreover, it is crucial to investigate molecular and cellular mechanisms to gain understanding of the biochemical pathways that led to the deactivation of microorganisms and lentivirus. These studies might also offer insights into the large differences in the deactivation efficiency between bacteria (>99.9999%) and fungi spores treated with ENM devices.

Sustained concentration of Cu(I) and OH in the ENM devices

The redox pathways in the top triangular portion of Fig. 6 are intended to emphasize the crucial role that copper redox chemistry plays in the generation of ROS and RCS. Cu(0), Cu(I), and Cu(II) form three vertices of the triangle in Fig. 6. Cu(I) and Cu(II) represent sums of all cuprous and cupric species in the solution, respectively. Major redox reactions involving Cu(0/I/II) species are shown in Eqs. 18 to 25; however, these reactions are not intended to be an exhaustive list of reactions. E_0 is the standard reduction potential of the respective reaction. Specifically, Eq. 18 [battery-assisted Cu(II) reduction] and Eq. 20 (Walden reductor) are two major sources of Cu(I). HOCl generation (Eq. 17) can be another source of Cu(I), although its contribution to

the total Cu(I) was not investigated in the studies. Cu(I) was consumed by Eqs. 19 and 22 and through Cu(I)-induced production of ROS and RCS (Eqs. 4, 5, 8, 9, and 13).

We confine our discussion on Cu(I) because its presence is crucial to providing ENM antimicrobial and antiviral properties. Although the half-life of Cu(I) is relatively short (30 s to 3 min), the experiments confirmed that Cu(I) was produced over an extended duration of time in the solutions treated with ENM devices (Fig. 5). The [Cu(I)]- τ_{app} dependence results indicated that [Cu(I)] plateaued at $\tau_{app} \approx 45$ and \approx 1440 min for ENM_{0V} and ENM_{3V} treatments, respectively. Furthermore, both the pseudo-steady-state [Cu(I)]_{ss} and initial [Cu(I)] production rates for ENM_{3V} devices were significantly larger than those for the ENM_{0V} devices (Fig. 5). Thus, the contribution of the Cu(I)generation by the Walden reductor is limited during initial stages $(\tau_{app} < 60 \text{ min})$, whereas the dominant factor that contributed to long-term Cu(I) production with an enhanced rate is attributed to Cu(II) reduction by external batteries. Overall, these experimental results implied that efficient redox cycling of copper species $[Cu(0) \Rightarrow$ $Cu(I) \leftrightharpoons Cu(II)$, through electric polarization of the conductive surfaces, yielded Cu(I) generation for a long period of time

$$Cu(II) + e^- \rightarrow Cu(I)$$
 (18)
 $E_o = 0.159 \text{ V (external power)}$

$$Cu(I) + e^{-} \rightarrow Cu(0)$$

$$E_o = 0.159 \text{ V}$$
(19)

$$Cu(II) + Ag + 3Cl^{-} \rightarrow CuCl_{2}^{-} + AgCl^{-}$$

$$E_{o} = 0.231 \text{ V}$$
(20)

$$AgCl \rightarrow Ag + Cl^{-}$$

$$E_0 = 0.222 \text{ V}$$
(21)

$$Cu(I) + Cu(I) \rightarrow Cu(II) + Cu(0)$$

$$E_o = 0.361 \text{ V}$$
(22)

$$Cu(II) + 2e^{-} \rightarrow Cu(0)$$
 (23)
 $E_0 = 0.3419 \text{ V}$

$$Ag \rightarrow Ag^+ + e^-$$
 (24)
 $E_o = 0.7996 \text{ V (external power)}$

$$Ag^{+} + Cu(0) \rightarrow Ag + Cu(II)$$

$$E_o = 0.457 \text{ V}$$
(25)

From the previous discussion, it is clear that control over the distribution and concentration of Cu(II) dispersed in silver coatings is highly desirable to ensure consistent antimicrobial and antiviral performance of ENM devices. In the present studies, Cu(II) deposition in the ENM devices was accomplished by soaking the devices in a copper sulfate solution. Our EDS measurements revealed relatively less uniform Cu(II) distribution at the microscale dimension on the device surfaces (figs. S7 and S9). The deposition time and CuSO₄ concentration of the

deposition solution had only a minor effect on the distribution and concentration of Cu(II) on the devices. Enhanced uniform Cu(II) distribution and control over its concentration in the ENM devices can be accomplished by tuning the surface chemistry of the substrates and using other established deposition methods, such as chemical, electrochemical, magnetron sputtering, and chemical vapor deposition (111–113). Furthermore, more economical deposition methods that do not compromise adhesion and mechanical properties of the coating and substrates need to be studied. The deposition of Cu(I) and Cu(II) oxide NPs may also provide another venue for controlling the concentration and distribution of copper in the ENM devices (114).

Many Cu- and Ag-based NPs and coatings exhibiting antimicrobial properties have been demonstrated in the literature (19, 27, 31, 32, 39, 40). More extensive reviews that describe the synthesis and characterization of Cu- and Ag-based NPs and coatings and their utilization for antimicrobial properties are also available in the literature (19, 21, 22, 25, 115, 116). Table 3 provides a comparison of antimicrobial modes and performance of the present study with some previously published reports. Table 3 is not a comprehensive comparison but illustrates the main advantage of the present report, which is broadband deactivation of microorganisms and lentivirion in a relatively short time of treatment.

Metal	Antimicrobial mechanism	Results		
Ag-Ga (<i>120</i>)	ROS-induced disruption of the integrity of the cell membrane. Biochemical modifications of the bacteria due to the interaction with the Ag-Ga solution.	99% elimination rates for <i>S. aureus</i> and <i>P. aeruginosa</i> treated with concentrations of 16 μ g cm ⁻² for Ag and 176 μ g cm ⁻² for Ga for a treatment of $\tau_{app} = 24$ hours.		
Ag/Ru (121)	Disinfection of bacteria is attributed to the production of H_2O_2 and $O_2^{\bullet-}$.	A disinfection efficiency of 99.9999% for E. coli, P. aeruginosa, and Bacillus subtilis for $\tau_{app} = 60$ min.		
Ag (122)	Membrane damage is attributed to oxidative stress produced by silver.	Inhibition of $\Delta log \sim 6.5$ for <i>P. aeruginosa</i> for $ au_{app} = 18$ hours.		
Ag and Cu NPs (<i>32</i>)	Disruption of the integrity of the cell wall, protein denaturation, and death caused by the interaction of Ag ions on the bacterial cell wall.	Ag NPs and Cu NPs showed high antimicrobial activity against <i>E. coli, S. aureus,</i> and <i>B. subtilis.</i> $\tau_{app} = 24$ hours.		
CuO NPs (27)	Possible disruption of the cell membrane and enzyme function by metallic ions.	CuO NPs produced a reduction of viable bacterial cells, including AMR bacteria with $\tau_{app} = 4$ hours.		
CuO, NiO, ZnO, and Sb ₂ O ₃ NPs (<i>40</i>)	Intrinsic toxicity of the metal oxide particles was attributed to deactivation of the bacteria.	CuO NPs produced a high inhibition of <i>E. coli</i> at a concentration of 125 mg liter ⁻¹ at $\tau_{app} = 24$ hours		
Au NPs (38)	Functionalized Au NPs attributed to the cell mem- brane disruption of both Gram-positive and Gram- negative bacteria, causing toxicity to bacteria.	Functionalized Au NPs exhibited high inhibition against 11 clinical multidrug-resistant bacteria. $\tau_{app} = \text{overnight}.$		
Ag/Cu alloy (123)	Release of Cu ⁺ and metallic silver and Cu ⁺ /Ag galvanic coupling are attributed to antimicrobial properties of the Ag/Cu alloy.	Planktonic S. <i>aureus</i> cell growth show \sim 7- to 8-log reduction after treatment at τ_{app} = 24 hours.		
SiO ₂ -Cu NPs (124)	Activities attributed to the antimicrobial properties of copper metallic NPs.	SiO ₂ -Cu showed >90% bacterial reduction of <i>E. co.</i> and <i>S. aureus</i> . $\tau_{app} = 24$ hours.		
Cotton/Cu NPs (125)	Antibacterial activity due to Cu NP toxicity.	Cu NPs on cotton showed an 8-log A. Baumannii reduction at $\tau_{app} = 10$ min.		
Cu NPs (<i>126</i>)	Contact killing is attributed to the observed anti- bacterial properties.	S. aureus and E. coli treated with copper NPs deposited on cellulose films show a 5- to 6-log reduction. $\tau_{app} = 1$ hour.		
Cu/Ag NPs (<i>127</i>)	Binding of metallic particles to the cell wall and the interference of biochemical reactions after NP interactions are attributed to killing and inhibition of bacteria.	Cu/Ag NPs yielded higher antibacterial properties than either Cu NPs or Ag NPs. τ _{app} = 18 hours.		
Methyl methacrylate resin/Cu (128)	Disruption of cell membrane by the interaction of metal ions.	A 99.9% reduction in bacteria was observed after treatment with copper/methyl methacrylate surfaced. τ _{app} = 1 hour.		
Cu(II)/Ag coatings (this study)	Generation of ROS and RCS species mediated through Cu(I) deactivated bacteria, fungi, and lentivirion.	More than 6-log reduction of both Gram-positive and Gram-negative bacteria and deactivation of fungi and lentivirion after treatment with Cu(II) (15.7 ppm cm ⁻²) embedded in Ag coating was observed. $\tau_{app} < 10$ min.		
Cu(II)/Ag coatings (this study)	Generation of ROS and RCS species mediated through Cu(I) deactivated bacteria, fungi, and lentivirion.	More than 6-log reduction of both Gram-positive and Gram-negative bacteria and deactivation of fungi and lentivirion after treatment with Cu(II) (15.7 ppm cm $^{-2}$) embedded in Ag coating was observed. $\tau_{app} < 10$ min.		

ENM devices are composed of electrically polarized Cu(II)-Ag coating on surfaces. The ENM devices can be fabricated on a range of surfaces in multiple settings for applications in homes, restaurants, hospitals, public places (such as railway stations and airports), and industries. For examples, ENM devices can be incorporated on wearable masks, clothing, doorknobs, hospital furniture (handles and frames), toilet seats, and heating, venting, and air conditioning applications. In principle, any surface that is prone to biological contamination is a target for ENM. However, care should be taken to avoid undesirable effects of ENM devices in some situations. For example, it is important to avoid excessive generation of ROS and RCS for applications involving food, medicine, and eating applications. Furthermore, attention is also warranted regarding the useful lifetime of the working ENM devices. The ENM devices used in the studies were composed of ~90-nm-thick silver coatings, which were shown to generate sustained production of Cu(I) and OH in $[Cl^-] \approx 0.3$ mM solutions for an extended period (Fig. 5H). However, the useful lifetime of the ENM devices in highly concentrated salt solutions $([Cl^-] > 1 \text{ M})$ was severely affected (<30 min) due to corrosion of the conductive silver coatings. Thus, additional studies are needed to enhance the longevity and lifetime of the ENM devices for applications involving highly corrosive salt solutions.

A recent independent review by J. O'Neill predicted an additional 10 million annual death by 2050 because of AMR (117) and a projected global gross domestic product (GDP) loss of up to \$100 trillion during this period. Similar to climate change and access to clean water, AMR also poses a major challenge to humans (118). Understanding and managing AMR require careful coordinated actions from multiple sectors and constituents, and innovative strategies that are effective against a broad range of AMR are needed. Unlike antibiotics, which tend to deactivate microorganisms through specific molecular interactions, OH and HOCl react indiscriminately with microorganisms and viruses. Therefore, it will be interesting to investigate ROS- and RCS-producing ENM devices against multidrug-resistant bacteria, such as Clostridium perfringens, Salmonella, multidrug-resistant S. aureus, Bacillus cereus, Candida auris, and M2 inhibitors of virus-resistant influenza flu A. Although the deactivation of AMR by nanoscale species is reported in the literature (36, 38, 58), it is imperative to confirm the effectiveness of ENM devices against AMR.

Low-power ENM coatings composed of cupric salt and metallic silver exhibited effective deactivation of a broad range of microbes in less than 10 min of treatment. More than 6-log reduction of five different bacteria—both Gram-positive and Gram-negative—was observed when the bacterial cells were treated with ENM devices. Such ENM treatments were also effective against lentivirus and two medically relevant fungi. In situ hydrogen peroxide in micromolar concentrations was produced with the ENM treatment. The spectroscopic measurements confirmed micromolar cuprous ions in the ENM-treated solutions, which is key to sustainable production of highly reactive hydroxyl radicals and hypochlorous acid in the solution. The electron microscopy studies showed a substantial distortion of bacterial cells and release of intercellular material after ENM treatments. ENM uses an unconventional strategy by harnessing the electrical polarization of nanoscale metallic coatings to generate reactive oxygenated and chlorinated species for the deactivation of broad-spectrum microorganisms and lentivirus. ENM devices can be fabricated at a relatively low cost using accessible materials, allowing their applications at home and in the industry and hospital, for combating the spread of infectious

diseases. Overall, these studies introduce a new tool in managing infections caused by microorganisms and viruses.

MATERIALS AND METHODS

Materials

The control polypropylene surfaces were taken from disposable earloop 3-Ply face masks (BLSCODE, China). Copper sulfate, BCS, coumarin, potassium iodide, sodium hydroxide, ammonium molybdate, hydrogen peroxide (30%), and all the solvents used in the experiments were purchased from Fisher Scientific. Fluorescein (Eastman Chemical), pH indicator paper (0–14) type CF (Whatman International Ltd.), PHP100 indicator paper (United Scientific Supplies), ascorbic acid (Sigma-Aldrich), cytochrome c (Sigma-Aldrich), Acid Red 94, *N,N*-dimethyl-4-nitrosoaniline (TCI), and potassium hydrogen phthalate (TCI) were purchased from respective vendors. Plain microscope slides (75 mm × 50 mm × 1 mm) were obtained from PRO Advantage NDC Company. 3M copper electrical tape (model number 1245) was used for all experiments.

Fabrication of ENM

The polypropylene surfaces were immersed in a $0.1~M~CuSO_4$ solution for 1 hour. Then, ~80- to 100-nm-thick coating of silver was sputtered on both sides of the Cu-containing surfaces. Conducting silver leads were adhered to the ENM devices using silver paste. Either alkaline batteries or commercial solar cells irradiated with LED (70 W, Utilitech) were used for the electric polarization of the ENM devices. ENM devices were also fabricated on household air filters, cellulose filter paper, and hand paper towels using the same method of preparation. More details on the fabrication and characterization can be found in the Supplementary Materials.

Spectroscopic characterization Quantification of Cu(I) using BCS

Cu(I) was quantified spectroscopically using the BCS method (92, 93). Briefly, control, Ag, ENM_{0V}, and ENM_{3V} devices of a known device area were soaked in 2 ml of a freshly prepared 0.25 mM BCS solution kept in a quartz cuvette for varying τ_{app} . The electronic absorbance measurements of the Cu(I)-BCS complex were performed in the dark using a Cary 100 spectrometer (slit width = 0.33 nm; scanning speed = 200 nm min⁻¹). The Cu(I) concentration in solutions were estimated using a Cu(I)-BCS complex molar absorption coefficient of 12,250 M⁻¹ cm⁻¹ at λ = 483 nm (92, 93).

Spectroscopic quantification of hydrogen peroxide

The concentration of hydrogen peroxide in the solutions was spectroscopically estimated using the I_3^- method reported by Klassen $\it et~al.~(94).~Cu(II),~Ag,~ENM_{0V},~and~ENM_{3V}~devices of known surface area were soaked in deionized water for a given <math display="inline">\tau_{app}=0$ to 30 min. Then, 2 ml of an ENM-treated solution was mixed with 1 ml of reagent I [consisting of potassium iodide (66 g liter $^{-1}$), sodium hydroxide (2 g liter $^{-1}$), and ammonium molybdate tetrahydrate (0.2 g liter $^{-1}$)] and 1 ml of the aqueous potassium hydrogen phthalate buffer (20 g liter $^{-1}$) in the dark for 5 min. The quantification of H_2O_2 concentration was performed by measuring I_3^- absorption at 351 nm ($\epsilon=25,800~M^{-1}~cm^{-1}$) using a Cary 100 spectrometer (94).

Hydroxyl radical detection using coumarin as a fluorescent probe

*OH was detected by the formation of 7HC in a coumarin solution (96). ENM_{0V} and ENM_{3V} devices (area = 16 cm²) were placed in

8 ml of a freshly prepared 1 mM aqueous coumarin solution. The fluorescence emission measurements were taken at various τ_{app} using an LS55 Perkin Elmer spectrometer ($\lambda_{ex} = 330$ nm, scan rate of 200 nm min⁻¹, and excitation and emission slit widths = 15 nm). The 'OH concentration in the ENM-treated solutions was estimated by using a calibration curve generated between [7HC] and emission intensity (fig. S22).

Spectroscopic measurements of hydroxyl radicals using N,N-dimethyl-4-nitrosoaniline

The 'OH concentration in ENM-treated solutions was also estimated using a reaction between 'OH and NDA (95). The devices were placed in 6 ml of 1 μ M NDA solution, and the decrease in the absorbance of the peak at 440 nm (ϵ = 34,200 M⁻¹ cm⁻¹) was used to quantify the 'OH concentration in the experiments (95).

Quantification of HOCI

Six milliliters of aqueous solutions containing 0.25 ml of o-tolidine was treated with 1-cm² ENM_{0V} and ENM_{3V} devices for $\tau_{app} = 5$, 30, and 60 min. The colorless solution changed to yellow with ENM treatment due to the formation of holoquinone (97, 119). The electronic absorbance of the solutions was taken using a Cary 100 spectrometer. The HOCl concentration in the solutions was estimated by using a molar extinction coefficient of 14,720 M⁻¹ cm⁻¹ at $\lambda = 437$ nm (fig. S23).

Electron and atomic force microscopy measurements

The fabrication of ENM devices at various stages was characterized by using SEM and EDS. Thermo Fisher Quanta FEG 450 and X Max 50 (Oxford) were used to acquire SEM and EDS measurements, respectively. An accelerating voltage of either 20 or 30 kV, a spot size of 3.5, and a working distance of 6 to 10 mm were used for the SEM measurements. The atomic force microscopy (AFM) measurements for silver thickness and NP distribution were performed using a Bruker Dimension V Icon AFM instrument. ScanAsyst-Air probes (resonance frequency = 45 to 95 kHz, length = 100 to 130 μm , width = 20 to 30 μm , and spring constant = 0.2 to 0.8 N m $^{-1}$) were used for the measurements.

Evaluation of bacteria, fungi spores, and lentivirus treatments with ENM

Approximately 100 µl of bacteria or fungi spores was placed on ENM devices that were polarized at an appropriate E_{app} for τ_{app} duration. Ninety microliters of the bacteria mixture was then extracted from the ENM devices for growth studies. The growth media contained sterilized agar in Luria-Bertani + glucose media for SIUC2 and SIUC11, glucose minimal media for A. fumigatus, and yeast extract-peptone-dextrose for C. albicans (Supplementary Materials). S. aureus, A. baumannii, and P. aeruginosa treated with ENM devices were grown in tryptic soy broth medium. The agar plates were incubated for 24 hours at 37°C prior to counting the colonies. Aseptic conditions were maintained at all times during experiments. All experiments were performed in at least triplicates. Cells were counted manually, and statistical analysis was performed using GraphPad Prism (see below). Detailed procedures for the treatment of lentivirion with Ag devices, HEK293T transduction with lentivirion, and the lentivirus deactivation efficiency studies are provided in the Supplementary Materials.

Data analysis

Deactivation efficiency (η) and Δ log were estimated using Eqs. 2 and 3, respectively. For bacteria and fungi spore experiments, a one-way analysis of variance (ANOVA) was performed to analyze the data, and a Tukey's multiple comparison test was used to compare

means when differences were found using GraphPad Prism (Dotmatics). When bacterial cells were not detected after 24 hours of growth period, CFU ml⁻¹ = 1 (i.e., log1 = 0) was assumed to avoid error in the Δ log calculations. The SD for the Δ log (S_{LR}) was estimated using $S_{LR} = [(S_{\text{control}}^2/n) + (S_{\text{device}}^2/m)]^{1/2}$, where S_{control} and S_{device} are SDs for the log reductions for the control and device treatments, respectively, and n and m are the number of control and ENM device treatments, respectively. For lentivirus studies, P values were estimated from three independent experiments using a two-way ANOVA test followed by Bonferroni correction.

Supplementary Materials

This PDF file includes:

Supplementary Materials and Methods Figs. S1 to S27 Tables S1 to S7 References

REFERENCES AND NOTES

- GBD 2019 Diseases and Injuries Collaborators, Global burden of 369 diseases and injuries in 204 countries and territories, 1990-2019: A systematic analysis for the Global Burden of Disease Study 2019. Lancet 396, 1204–1222 (2020).
- GBD 2019 Diseases and Injuries Collaborators, Global mortality associated with 33 bacterial pathogens in 2019: A systematic analysis for the Global Burden of Disease Study 2019. Lancet 400, 2221–2248 (2022).
- Centers for Disease Control and Prevention, CDC Current Outbreak List (CDC, 2023); https://cdc.gov/outbreaks/index.html#.
- B. Balasubramaniam, Prateek, S. Ranjan, M. Saraf, P. Kar, S. P. Singh, V. K. Thakur, A. Singh, R. K. Gupta, Antibacterial and antiviral functional materials: Chemistry and biological activity toward tackling COVID-19-like pandemics. ACS Pharmacol. Transl. Sci. 4, 8–54 (2021).
- D. Wu, T. Wu, Q. Liu, Z. Yang, The SARS-CoV-2 outbreak: What we know. Int. J. Infect. Dis. 94, 44–48 (2020).
- E. M. Bunge, B. Hoet, L. Chen, F. Lienert, H. Weidenthaler, L. R. Baer, R. Steffen, The changing epidemiology of human monkeypox—A potential threat? A systematic review. *PLOS Negl. Trop. Dis.* 16, e0010141 (2022).
- J. P. Thornhill, S. Barkati, S. Walmsley, J. Rockstroh, A. Antinori, L. B. Harrison, R. Palich,
 A. Nori, I. Reeves, M. S. Habibi, V. Apea, C. Boesecke, L. Vandekerckhove, M. Yakubovsky,
 E. Sendagorta, J. L. Blanco, E. Florence, D. Moschese, F. M. Maltez, A. Goorhuis,
 V. Pourcher, P. Migaud, S. Noe, C. Pintado, F. Maggi, A. E. Hansen, C. Hoffmann,
 J. I. Lezama, C. Mussini, A. Cattelan, K. Makofane, D. Tan, S. Nozza, J. Nemeth, M. B. Klein,
 C. M. Orkin; SHARE-net Clinical Group, Monkeypox virus infection in humans across 16
 countries—April-June 2022. N. Engl. J. Med. 387, 679-691 (2022).
- C. Viboud, O. N. Bjørnstad, D. L. Smith, L. Simonsen, M. A. Miller, B. T. Grenfell, Synchrony, waves, and spatial hierarchies in the spread of influenza. *Science* 312, 447–451 (2006).
- B. J. Cowling, D. K. M. Ip, V. J. Fang, P. Suntarattiwong, S. J. Olsen, J. Levy, T. M. Uyeki, G. M. Leung, J. S. Malik Peiris, T. Chotpitayasunondh, H. Nishiura, J. Mark Simmerman, Aerosol transmission is an important mode of influenza A virus spread. *Nat. Commun.* 4, 1935 (2013).
- X. Du, A. A. King, R. J. Woods, M. Pascual, Evolution-informed forecasting of seasonal influenza A (H3N2). Sci. Transl. Med. 9, eaan5325 (2017).
- A. Düx, S. Lequime, L. V. Patrono, B. Vrancken, S. Boral, J. F. Gogarten, A. Hilbig, D. Horst, K. Merkel, B. Prepoint, S. Santibanez, J. Schlotterbeck, M. A. Suchard, M. Ulrich, N. Widulin, A. Mankertz, F. H. Leendertz, K. Harper, T. Schnalke, P. Lemey, S. Calvignac-Spencer, Measles virus and rinderpest virus divergence dated to the sixth century BCE. Science 368, 1367–1370 (2020).
- W. Yang, Transmission dynamics of and insights from the 2018–2019 measles outbreak in New York City: A modeling study. Sci. Adv. 6, eaaz4037 (2020).
- C. A. Michael, D. Dominey-Howes, M. Labbate, The antimicrobial resistance crisis: Causes, consequences, and management. Front. Public Health 2, 145 (2014).
- World Health Organization, Antimicrobial Resistance: Global Report on Surveillance (World Health Organization, 2014).
- F. Micoli, F. Bagnoli, R. Rappuoli, D. Serruto, The role of vaccines in combatting antimicrobial resistance. Nat. Rev. Microbiol. 19, 287–302 (2021).
- M. Lipsitch, M. H. Samore, Antimicrobial use and antimicrobial resistance: A population perspective. Emerg. Infect. Dis. 8, 347–354 (2002).
- J. Davies, D. Davies, Origins and evolution of antibiotic resistance. Microbiol. Mol. Biol. Rev. 74, 417–433 (2010).

SCIENCE ADVANCES | RESEARCH ARTICLE

- 18. C. L. Ventola, The antibiotic resistance crisis: Part 1: Causes and threats. P. T. 40, 277–283 (2015).
- M. Cloutier, D. Mantovani, F. Rosei, Antibacterial coatings: Challenges, perspectives, and opportunities. *Trends Biotechnol.* 33, 637–652 (2015).
- M. Salwiczek, Y. Qu, J. Gardiner, R. A. Strugnell, T. Lithgow, K. M. McLean, H. Thissen, Emerging rules for effective antimicrobial coatings. *Trends Biotechnol.* 32, 82–90 (2014).
- M. L. Knetsch, L. H. Koole, New strategies in the development of antimicrobial coatings: The example of increasing usage of silver and silver nanoparticles. *Polymers* 3, 340–366 (2011).
- 22. J. C. Tiller, Antimicrobial surfaces in *Bioactive Surfaces* (Springer, 2011), pp. 193–217.
- I. W. Hamley, Small bioactive peptides for biomaterials design and therapeutics. Chem. Rev. 117, 14015–14041 (2017).
- B. Song, E. Zhang, X. Han, H. Zhu, Y. Shi, Z. Cao, Engineering and application perspectives on designing an antimicrobial surface. ACS Appl. Mater. Interfaces 12, 21330–21341 (2020).
- S. Eckhardt, P. S. Brunetto, J. Gagnon, M. Priebe, B. Giese, K. M. Fromm, Nanobio silver: Its interactions with peptides and bacteria, and its uses in medicine. *Chem. Rev.* 113, 4708–4754 (2013).
- M. Garland, S. Loscher, M. Bogyo, Chemical strategies to target bacterial virulence. Chem. Rev. 117, 4422–4461 (2017).
- G. Ren, D. Hu, E. W. C. Cheng, M. A. Vargas-Reus, P. Reip, R. P. Allaker, Characterisation of copper oxide nanoparticles for antimicrobial applications. *Int. J. Antimicrob. Agents* 33, 587–590 (2009).
- M. Krishnamoorthy, S. Hakobyan, M. Ramstedt, J. E. Gautrot, Surface-initiated polymer brushes in the biomedical field: Applications in membrane science, biosensing, cell culture, regenerative medicine and antibacterial coatings. Chem. Rev. 114, 10976–11026 (2014).
- E.-R. Kenawy, S. D. Worley, R. Broughton, The chemistry and applications of antimicrobial polymers: A state-of-the-art review. *Biomacromolecules* 8, 1359–1384 (2007).
- J. S. Kim, E. Kuk, K. N. Yu, J.-H. Kim, S. J. Park, H. J. Lee, S. H. Kim, Y. K. Park, Y. H. Park, C.-Y. Hwang, Y.-K. Kim, Y.-S. Lee, D. H. Jeong, M.-H. Cho, Antimicrobial effects of silver nanoparticles. *Nanomedicine* 3, 95–101 (2007).
- Y. Li, W. Zhang, J. Niu, Y. Chen, Mechanism of photogenerated reactive oxygen species and correlation with the antibacterial properties of engineered metal-oxide nanoparticles. ACS Nano 6, 5164–5173 (2012).
- J. P. Ruparelia, A. K. Chatterjee, S. P. Duttagupta, S. Mukherji, Strain specificity in antimicrobial activity of silver and copper nanoparticles. *Acta Biomater.* 4, 707–716 (2008)
- M. Rai, A. Yadav, A. Gade, Silver nanoparticles as a new generation of antimicrobials. Biotechnol. Adv. 27, 76–83 (2009).
- K. Zheng, M. I. Setyawati, D. T. Leong, J. Xie, Antimicrobial gold nanoclusters. ACS Nano 11, 6904–6910 (2017).
- Y. Zhang, T. P. Shareena Dasari, H. Deng, H. Yu, Antimicrobial activity of gold nanoparticles and ionic gold. *J. Environ. Sci. Health C Environ. Carcinog. Ecotoxicol. Rev.* 33, 286–327 (2015).
- J. M. V. Makabenta, A. Nabawy, C.-H. Li, S. Schmidt-Malan, R. Patel, V. M. Rotello, Nanomaterial-based therapeutics for antibiotic-resistant bacterial infections. *Nat. Rev. Microbiol.* 19, 23–36 (2021).
- A. Gupta, W. Ndugire, C.-M. Hirschbiegel, L. Grigely, V. M. Rotello, Interfacing nanomaterials with biology through ligand engineering. Acc. Chem. Res. 56, 2151–2169 (2023).
- X. Li, S. M. Robinson, A. Gupta, K. Saha, Z. Jiang, D. F. Moyano, A. Sahar, M. A. Riley, V. M. Rotello, Functional gold nanoparticles as potent antimicrobial agents against multi-drug-resistant bacteria. ACS Nano 8, 10682–10686 (2014).
- M. Heinlaan, A. Ivask, I. Blinova, H.-C. Dubourguier, A. Kahru, Toxicity of nanosized and bulk ZnO, CuO and TiO₂ to bacteria Vibrio fischeri and crustaceans Daphnia magna and Thamnocephalus platyurus. Chemosphere 71, 1308–1316 (2008).
- Y.-W. Baek, Y.-J. An, Microbial toxicity of metal oxide nanoparticles (CuO, NiO, ZnO, and Sb₂O₃) to Escherichia coli, Bacillus subtilis, and Streptococcus aureus. Sci. Total Environ. 409, 1603–1608 (2011).
- Y. H. Leung, A. M. C. Ng, X. Xu, Z. Shen, L. A. Gethings, M. T. Wong, C. M. N. Chan, M. Y. Guo, Y. H. Ng, A. B. Djurišić, P. K. H. Lee, W. K. Chan, L. H. Yu, D. L. Phillips, A. P. Y. Ma, F. C. C. Leung, Mechanisms of antibacterial activity of MgO: Non-ROS mediated toxicity of MgO nanoparticles towards *Escherichia coli*. *Small* 10, 1171–1183 (2014).
- M. Arakha, S. Pal, D. Samantarrai, T. K. Panigrahi, B. C. Mallick, K. Pramanik, B. Mallick, S. Jha, Antimicrobial activity of iron oxide nanoparticle upon modulation of nanoparticle-bacteria interface. Sci. Rep. 5, 14813 (2015).
- A. Jesline, N. P. John, P. M. Narayanan, C. Vani, S. Murugan, Antimicrobial activity of zinc and titanium dioxide nanoparticles against biofilm-producing methicillin-resistant Staphylococcus aureus. Appl. Nanosci. 5, 157–162 (2015).
- T. C. Long, N. Saleh, R. D. Tilton, G. V. Lowry, B. Veronesi, Titanium dioxide (P25) produces reactive oxygen species in immortalized brain microglia (BV2): Implications for nanoparticle neurotoxicity. *Environ. Sci. Technol.* 40, 4346–4352 (2006).
- T. Xia, M. Kovochich, M. Liong, L. Mädler, B. Gilbert, H. Shi, J. I. Yeh, J. I. Zink, A. E. Nel, Comparison of the mechanism of toxicity of zinc oxide and cerium oxide

- nanoparticles based on dissolution and oxidative stress properties. ACS Nano 2, 2121–2134 (2008).
- Z. Emami-Karvani, P. Chehrazi, Antibacterial activity of ZnO nanoparticle on grampositive and gram-negative bacteria. Afr. J. Microbiol. Res. 5, 1368–1373 (2011).
- M. J. Hajipour, K. M. Fromm, A. Akbar Ashkarran, D. Jimenez de Aberasturi,
 I. R. Larramendi, T. Rojo, V. Serpooshan, W. J. Parak, M. Mahmoudi, Antibacterial properties of nanoparticles. *Trends Biotechnol.* 30, 499–511 (2012).
- L. Wang, C. Hu, L. Shao, The antimicrobial activity of nanoparticles: Present situation and prospects for the future. *Int. J. Nanomedicine* 12, 1227–1249 (2017).
- Y. Nosaka, A. Y. Nosaka, Generation and detection of reactive oxygen species in photocatalysis. Chem. Rev. 117, 11302–11336 (2017).
- C. C. Winterbourn, Reconciling the chemistry and biology of reactive oxygen species. Nat. Chem. Biol. 4, 278–286 (2008).
- J.T. Hancock, R. Desikan, S. J. Neill, Role of reactive oxygen species in cell signalling pathways. *Biochem. Soc. Trans.* 29, 345–349 (2001).
- 52. M. P. Murphy, How mitochondria produce reactive oxygen species. *Biochem. J.* **417**, 1–13
- V. J. Thannickal, B. L. Fanburg, Reactive oxygen species in cell signaling. Am. J. Physiol. Lung Cell. Mol. Physiol. 279, L1005–L1028 (2000).
- J. F. Turrens, Mitochondrial formation of reactive oxygen species. J. Physiol. 552, 335–344 (2003).
- 55. T. Finkel, Signal transduction by reactive oxygen species. J. Cell Biol. 194, 7-15 (2011).
- J. A. Lemire, J. J. Harrison, R. J. Turner, Antimicrobial activity of metals: Mechanisms, molecular targets and applications. *Nat. Rev. Microbiol.* 11, 371–384 (2013).
- Y. Si, Z. Zhang, W. Wu, Q. Fu, K. Huang, N. Nitin, B. Ding, G. Sun, Daylight-driven rechargeable antibacterial and antiviral nanofibrous membranes for bioprotective applications. Sci. Adv. 4, eaar5931 (2018).
- A. L. Santos, D. Liu, A. K. Reed, A. M. Wyderka, A. van Venrooy, J. T. Li, V. D. Li, M. Misiura,
 O. Samoylova, J. L. Beckham, C. Ayala-Orozco, A. B. Kolomeisky, L. B. Alemany, A. Oliver,
 G. P. Tegos, J. M. Tour, Light-activated molecular machines are fast-acting broad-spectrum antibacterials that target the membrane. Sci. Adv. 8, eabm2055 (2022).
- A. P. Richter, J. S. Brown, B. Bharti, A. Wang, S. Gangwal, K. Houck, E. A. Cohen Hubal, V. N. Paunov, S. D. Stoyanov, O. D. Velev, An environmentally benign antimicrobial nanoparticle based on a silver-infused lignin core. *Nat. Nanotechnol.* 10, 817–823 (2015).
- W. A. Velema, J. P. van der Berg, M. J. Hansen, W. Szymanski, A. J. M. Driessen, B. L. Feringa, Optical control of antibacterial activity. *Nat. Chem.* 5, 924–928 (2013).
- Y. Zhao, Y. Tian, Y. Cui, W. Liu, W. Ma, X. Jiang, Small molecule-capped gold nanoparticles as potent antibacterial agents that target gram-negative bacteria. *J. Am. Chem. Soc.* 132, 12349–12356 (2010).
- J. J. Harrison, H. Ceri, C. A. Stremick, R. J. Turner, Biofilm susceptibility to metal toxicity. Environ. Microbiol. 6, 1220–1227 (2004).
- V. García-López, F. Chen, L. G. Nilewski, G. Duret, A. Aliyan, A. B. Kolomeisky, J. T. Robinson, G. Wang, R. Pal, J. M. Tour, Molecular machines open cell membranes. Nature 548, 567–572 (2017).
- E. P. Ivanova, J. Hasan, H. K. Webb, G. Gervinskas, S. Juodkazis, V. K. Truong, A. H. F. Wu, R. N. Lamb, V. A. Baulin, G. S. Watson, J. A. Watson, D. E. Mainwaring, R. J. Crawford, Bactericidal activity of black silicon. *Nat. Commun.* 4, 2838 (2013).
- P. Chen, J. Lang, Y. Zhou, A. Khlyustova, Z. Zhang, X. Ma, S. Liu, Y. Cheng, R. Yang, An imidazolium-based zwitterionic polymer for antiviral and antibacterial dual functional coatings. Sci. Adv. 8, eabl8812 (2022).
- C. M. Courtney, S. M. Goodman, T. A. Nagy, M. Levy, P. Bhusal, N. E. Madinger,
 C. S. Detweiler, P. Nagpal, A. Chatterjee, Potentiating antibiotics in drug-resistant clinical isolates via stimuli-activated superoxide generation. *Sci. Adv.* 3, e1701776 (2017).
- C.-Y. Chen, H. Yin, X. Chen, T.-H. Chen, H.-M. Liu, S.-S. Rao, Y.-J. Tan, Y.-X. Qian, Y.-W. Liu, X.-K. Hu, M.-J. Luo, Z.-X. Wang, Z.-Z. Liu, J. Cao, Z.-H. He, B. Wu, T. Yue, Y.-Y. Wang, K. Xia, Z.-W. Luo, Y. Wang, W.-Y. Situ, W.-E. Liu, S.-Y. Tang, H. Xie, Ångstrom-scale silver particle-embedded carbomer gel promotes wound healing by inhibiting bacterial colonization and inflammation. Sci. Adv. 6, eaba0942 (2020).
- J. W. Moffett, R. G. Zika, Reaction kinetics of hydrogen peroxide with copper and iron in seawater. Environ. Sci. Technol. 21, 804–810 (1987).
- D. Meyerstein, Re-examining Fenton and Fenton-like reactions. Nat. Rev. Chem. 5, 595–597 (2021).
- K. Frenkel, F. Blum, W. Troll, Copper ions and hydrogen peroxide form hypochlorite from NaCl thereby mimicking myeloperoxidase. J. Cell. Biochem. 30, 181–193 (1986).
- J. W. Moffett, R. G. Zika, Oxidation kinetics of Cu(l) in seawater: Implications for its existence in the marine environment. *Mar. Chem.* 13, 239–251 (1983).
- M. R. Gunther, P. M. Hanna, R. P. Mason, M. S. Cohen, Hydroxyl radical formation from cuprous ion and hydrogen peroxide: A spin-trapping study. *Arch. Biochem. Biophys.* 316, 515–522 (1995)
- X. Yuan, A. N. Pham, G. Xing, A. L. Rose, T. D. Waite, Effects of pH, chloride, and bicarbonate on Cu(l) oxidation kinetics at circumneutral pH. *Environ. Sci. Technol.* 46, 1527–1535 (2012).

SCIENCE ADVANCES | RESEARCH ARTICLE

- R. D. Gray, Kinetics of oxidation of copper(I) by molecular oxygen in perchloric acid-acetonitrile solutions. J. Am. Chem. Soc. 91, 56–62 (1969).
- A. D. Zuberbühler, Cuprous complexes and dioxygen, VII. Competition between one- and two-electron reduction of O₂ in the autoxidation of Cu(1-methyl-2-hydroxymethylimidazole)₂⁺. Helv. Chim. Acta 59, 1448–1459 (1976).
- P. M. Wood, The redox potential of the system oxygen—Superoxide. FEBS Lett. 44, 22–24 (1974).
- I. Pecht, M. Anbar, The oxidation of bis(bipyridyl)copper(I) ions by oxygen and by hydrogen peroxide. J. Chem. Soc. A 1968, 1902–1904 (1968).
- A. L. Crumbliss, A. T. Poulos, Kinetics of oxidation of a cuprous 2,2',2"-terpyridine complex by molecular oxygen. *Inorg. Chem.* 14, 1529–1534 (1975).
- A. J. Bard, R. Parsons, J. Jordan, Standard Potentials in Aqueous Solution (Marcel Dekker Inc., 1985), pp. 287–321.
- K. Kondo, T. Nakamura, N. Okamoto, Correlation between Cu (I)-complexes and filling of via cross sections by copper electrodeposition. J. Appl. Electrochem. 39, 1789–1795 (2009)
- G. H. Walden Jr., L. P. Hammett, S. M. Edmonds, Phenanthroline-ferrous ion. III. A silver reductor. The direct determination of iron in the presence of vanadium¹. J. Am. Chem. Soc. 56, 350–353 (1934).
- N. Birnbaum, S. M. Edmonds, New applications of the silver reductor. *Ind. Eng. Chem. Anal. Ed.* 12, 155–157 (1940).
- J. N. Pendleton, S. P. Gorman, B. F. Gilmore, Clinical relevance of the ESKAPE pathogens. Expert Rev. Anti Infect. Ther. 11, 297–308 (2013).
- Y. Sato, Y. Unno, C. Miyazaki, T. Ubagai, Y. Ono, Multidrug-resistant Acinetobacter baumannii resists reactive oxygen species and survives in macrophages. Sci. Rep. 9, 17462 (2019).
- S.-H. Gao, L. Fan, L. Peng, J. Guo, M. Agulló-Barceló, Z. Yuan, P. L. Bond, Determining multiple responses of *Pseudomonas aeruginosa* PAO1 to an antimicrobial agent, free nitrous acid. *Environ. Sci. Technol.* 50, 5305–5312 (2016).
- Z. Chen, P. Yang, Z. Yuan, J. Guo, Aerobic condition enhances bacteriostatic effects of silver nanoparticles in aquatic environment: An antimicrobial study on Pseudomonas aeruginosa. Sci. Rep. 7, 7398 (2017).
- P. Wiemann, A. Perevitsky, F. Y. Lim, Y. Shadkchan, B. P. Knox, J. A. Landero Figueora, T. Choera, M. Niu, A. J. Steinberger, M. Wüthrich, R. A. Idol, B. S. Klein, M. C. Dinauer, A. Huttenlocher, N. Osherov, N. P. Keller, *Aspergillus fumigatus* copper export machinery and reactive oxygen intermediate defense counter host copper-mediated oxidative antimicrobial offense. *Cell Rep.* 19, 1008–1021 (2017).
- L. Chen, P. J. Jensik, J. T. Alaimo, M. Walkiewicz, S. Berger, E. Roeder, E. A. Faqeih, J. A. Bernstein, A. C. M. Smith, S. V. Mullegama, D. W. Saffen, S. H. Elsea, Functional analysis of novel DEAF1 variants identified through clinical exome sequencing expands DEAF1-associated neurodevelopmental disorder (DAND) phenotype. *Hum. Mutat.* 38, 1774–1785 (2017).
- A. Gomes, E. Fernandes, J. L. F. C. Lima, Fluorescence probes used for detection of reactive oxygen species. J. Biochem. Biophys. Methods 65, 45–80 (2005).
- F. C. Fang, Antimicrobial reactive oxygen and nitrogen species: Concepts and controversies. Nat. Rev. Microbiol. 2, 820–832 (2004).
- M. J. Gray, W.-Y. Wholey, U. Jakob, Bacterial responses to reactive chlorine species. Annu. Rev. Microbiol. 67, 141–160 (2013).
- D. Blair, H. Diehl, Bathophenanthrolinedisulphonic acid and bathocuproinedisulphonic acid, water soluble reagents for iron and copper. *Talanta* 7, 163–174 (1961).
- C. Campos, R. Guzmán, E. López-Fernández, Á. Casado, Evaluation of the copper(II) reduction assay using bathocuproinedisulfonic acid disodium salt for the total antioxidant capacity assessment: The CUPRAC–BCS assay. Anal. Biochem. 392, 37–44 (2009).
- N. V. Klassen, D. Marchington, H. C. E. McGowan, H₂O₂ determination by the I³⁻ method and by KMnO₄ titration. *Anal. Chem.* 66, 2921–2925 (1994).
- I. Kraljić, C. N. Trumbore, p-Nitrosodimethylaniline as an OH radical scavenger in radiation chemistry¹. J. Am. Chem. Soc. 87, 2547–2550 (1965).
- K.-i. Ishibashi, A. Fujishima, T. Watanabe, K. Hashimoto, Detection of active oxidative species in TiO₂ photocatalysis using the fluorescence technique. *Electrochem. Commun.* 2, 207–210 (2000).
- D. Tarvin, H. R. Todd, A. M. Buswell, The determination of free chlorine. J. Am. Water Works Assoc. 26, 1645–1662 (1934).
- 98. B. H. J. Bielski, D. E. Cabelli, R. L. Arudi, A. B. Ross, Reactivity of HO₂/O⁻₂ radicals in aqueous solution. *J. Phys. Chem. Ref. Data Monogr.* **14**, 1041–1100 (1985).
- O. C. Zafiriou, B. M. Voelker, D. L. Sedlak, Chemistry of the superoxide radical (O₂⁻) in seawater: Reactions with inorganic copper complexes. *J. Phys. Chem. A* 102, 5693–5700 (1998).
- D. He, A. M. Jones, S. Garg, A. N. Pham, T. D. Waite, Silver nanoparticle–reactive oxygen species interactions: Application of a charging–discharging model. J. Phys. Chem. C 115, 5461–5468 (2011).
- T. C. Dakal, A. Kumar, R. S. Majumdar, V. Yadav, Mechanistic basis of antimicrobial actions of silver nanoparticles. Front. Microbiol. 7, 1831 (2016).

- T. Liu, B. Xiao, F. Xiang, J. Tan, Z. Chen, X. Zhang, C. Wu, Z. Mao, G. Luo, X. Chen, J. Deng, Ultrasmall copper-based nanoparticles for reactive oxygen species scavenging and alleviation of inflammation related diseases. *Nat. Commun.* 11, 2788 (2020).
- G. R. Buettner, The pecking order of free radicals and antioxidants: Lipid peroxidation, α-tocopherol, and ascorbate. Arch. Biochem. Biophys. 300, 535–543 (1993).
- K. M. Sutherland, S. D. Wankel, C. M. Hansel, Dark biological superoxide production as a significant flux and sink of marine dissolved oxygen. *Proc. Natl. Acad. Sci. U.S.A.* 117, 3433–3439 (2020).
- A. U. Khan, M. Kasha, Singlet molecular oxygen in the Haber-Weiss reaction. Proc. Natl. Acad. Sci. U.S.A. 91, 12365–12367 (1994).
- R. Roots, S. Okada, Estimation of life times and diffusion distances of radicals involved in X-ray-induced DNA strand breaks or killing of mammalian cells. Radiat. Res. 64, 306–320 (1975).
- F. J. Millero, The effect of ionic interactions on the oxidation of metals in natural waters. Geochim. Cosmochim. Acta 49, 547–553 (1985).
- A. Fontana, J. van Muylder, R. Winand, Etablissement de diagrammes tension-pH cinetiques du cuivre en milieu de chlorures. Electrochim. Acta 30, 641–647 (1985).
- J. M. Diaz, C. M. Hansel, B. M. Voelker, C. M. Mendes, P. F. Andeer, T. Zhang, Widespread production of extracellular superoxide by heterotrophic bacteria. *Science* 340, 1223–1226 (2013).
- M. Okuda, T. Tsuruta, K. Katayama, Lifetime and diffusion coefficient of active oxygen species generated in TiO₂ sol solutions. Phys. Chem. Chem. Phys. 11, 2287–2292 (2009)
- 111. H. Pierson, Handbook of Chemical Vapor Deposition (CVD) Principles, Technology, and Applications (Noyes Publications, ed. 2, 1999), pp. 506.
- G. O. Mallory, J. B. Hajdu, Electroless Plating: Fundamentals and Applications (Noyce Publications/William Andrew Publications, 1990).
- 113. M. Schlesinger, M. Paunovic, Modern Electroplating (Wiley, 2011).
- H. L. Karlsson, P. Cronholm, J. Gustafsson, L. Möller, Copper oxide nanoparticles are highly toxic: A comparison between metal oxide nanoparticles and carbon nanotubes. *Chem. Res. Toxicol.* 21, 1726–1732 (2008).
- M. B. Gawande, A. Goswami, F. X. Felpin, T. Asefa, X. Huang, R. Silva, X. Zou, R. Zboril, R. S. Varma, Cu and Cu-based nanoparticles: Synthesis and applications in catalysis. Chem. Rev. 116, 3722–3811 (2016).
- S. J. Soenen, W. J. Parak, J. Rejman, B. Manshian, (Intra)cellular stability of inorganic nanoparticles: Effects on cytotoxicity, particle functionality, and biomedical applications. Chem. Rev. 115, 2109–2135 (2015).
- J. O'Neill, Tackling Drug-Resistant Infections Globally: Final Report and Recommendations (Review on Antimicrobial Resistance, 2016); http://amr-review.org/ sites/default/files/160525_Final%20paper_with%20cover.pdf.
- L. S. J. Roope, R. D. Smith, K. B. Pouwels, J. Buchanan, L. Abel, P. Eibich, C. C. Butler, P. S. Tan, A. S. Walker, J. V. Robotham, S. Wordsworth, The challenge of antimicrobial resistance: What economics can contribute. *Science* 364, eaau4679 (2019).
- N. J. Nicolson, An evaluation of the methods for determining residual chlorine in water.
 Part I. Free chlorine. Analyst 90, 187–198 (1965).
- 120. T. T. Nguyen, P. Zhang, J. Bi, N. H. Nguyen, Y. Dang, Z. Xu, H. Wang, N. Ninan, R. Bright, T. Pham, C. K. Nguyen, Y. Sabri, M. T. Nguyen, J. Vongsvivut, Y. Zhao, K. Vasilev, V. K. Truong, Silver–gallium nano-amalgamated particles as a novel, biocompatible solution for antibacterial coatings. *Adv. Funct. Mater.* 2023, 2310539 (2023).
- 121. J. Yao, T. Jiang, Y. Ji, B. A. An, A. Koerdt, Z. Cai, C. Dong, Y. Ge, Z. Qi, Water-fueled autocatalytic bactericidal pathway based on e-Fenton-like reactions triggered by galvanic corrosion and extracellular electron transfer. J. Hazard. Mater. 440, 129730 (2022).
- J. Zhang, F. Qu, T. Liang, S. Lv, W. Li, Q. You, B. Chen, H. Xu, Novel e-polylysine/ polyethyleneimine-coated Ag nanoparticles for in vitro treatment of Pseudomonas aeruginosa. *Biochem. Eng. J.* 168, 107937 (2021).
- N. Ciacotich, R. U. Din, J. J. Sloth, P. Møller, L. Gram, An electroplated copper–silver alloy as antibacterial coating on stainless steel. Surf. Coat. Technol. 345, 96–104 (2018).
- A. Berendjchi, R. Khajavi, M. E. Yazdanshenas, Fabrication of superhydrophobic and antibacterial surface on cotton fabric by doped silica-based sols with nanoparticles of copper. Nanoscale Res. Lett. 6, 594 (2011).
- 125. N. C. Cady, J. L. Behnke, A. D. Strickland, Copper-based nanostructured coatings on natural cellulose: Nanocomposites exhibiting rapid and efficient inhibition of a multi-drug resistant wound pathogen, A. baumannii, and mammalian cell biocompatibility in vitro. Adv. Funct. Mater. 21, 2506–2514 (2011).
- B. Jia, Y. Mei, L. Cheng, J. Zhou, L. Zhang, Preparation of copper nanoparticles coated cellulose films with antibacterial properties through one-step reduction. ACS Appl. Mater. Interfaces 4, 2897–2902 (2012).
- H. R. Hong, J. Kim, C. H. Park, Facile fabrication of multifunctional fabrics: Use of copper and silver nanoparticles for antibacterial, superhydrophobic, conductive fabrics. RSC Adv. 8, 41782–41794 (2018).
- D. A. Montero, C. Arellano, M. Pardo, R. Vera, R. Gálvez, M. Cifuentes, M. A. Berasain, M. Gómez, C. Ramírez, R. M. Vidal, Antimicrobial properties of a novel copper-based composite coating with potential for use in healthcare facilities. *Antimicrob. Resist. Infect. Control* 8, 3 (2019).

SCIENCE ADVANCES | RESEARCH ARTICLE

- J. A. Frank, C. I. Reich, S. Sharma, J. S. Weisbaum, B. A. Wilson, G. J. Olsen, Critical evaluation of two primers commonly used for amplification of bacterial 16S rRNA genes. *Appl. Environ. Microbiol.* 74, 2461–2470 (2008).
- 130. P. M. Wood, The potential diagram for oxygen at pH 7. *Biochem. J.* **253**, 287–289 (1988).
- L. R. Faulkner, A. J. Bard, Electrochemical Methods: Fundamentals and Applications (Wiley, 2000), vol. 2, pp. 808.
- V. K. Sharma, F. J. Millero, Oxidation of copper(I) in seawater. Environ. Sci. Technol. 22, 768–771 (1988).

Acknowledgments: We would like to thank M. Kinsel and J. Harzan for helping with UV-Vis measurements, M. Brooks for performing the inductively coupled plasma optical emission spectrometry measurements, and R. Choudhary and P. Joshi for helping with microbiology experiments. A.Y.V.-L. acknowledges a dissertation research assistantship from the graduate school at the Southern Illinois University Carbondale and a Gower fellowship. Funding: We acknowledge the National Science Foundation (CHE-0748676, CHE-0959568, CHE-1905341, and CHE-1920255) (P.K.), National Institutes of Health (GM-106364) (P.K.), BARD (US4471-11F and US-4680-13C) (P.K.), the Office of the Vice Chancellor for Research (IMAGE Center), Cal A. Myers Institute (a seed grant) (P.K.), and SIUC system (an SIU System Collaborative Grant) (P.K. and M.E.O.) for partial funding of this work. Author contributions: Conceptualization: P.K., S.D.H.-B., M.E.O., A.Y.V.-L., M.A.A., J.M.V.-M., and M.Z. Methodology: P.K., A.Y.V.-L., M.A.A.,

J.M.V.-M., P.J.J., M.E.O., S.D.H.-B., G.M.K., and A.P. Investigation: P.K., A.Y.V.-L., M.A.A., M.E.O., P.J.J., J.M.V.-M., G.M.K., N.A.M., M.Z., T.S., M.G., and I.M.S. Supervision: P.K., S.D.H.-B., A.P., and B.M.G. Writing—original draft: A.Y.V.-L., M.A.A., P.K., and M.E.O. Writing—review and editing: P.K., A.Y.V.-L., M.A.A., R.K., a.M.G., N.A.M., and I.M.S. Resources: P.K., M.A.A., A.Y.V.-L., G.M.K., A.P., J.M.V.-M., G.M.K., B.M.G., N.A.M., and J.M.V.-M. Validation: P.K., G.M.K., M.Z., J.M.V.-M., S.D.H.-B., and T.S. Visualization: P.K., G.M.K., M.Z., A.P., and M.E.O. Project administration: P.K. and S.D.H.-B. Funding acquisition: P.K. and B.M.G. All authors have had access to the final draft of the manuscript. **Competing interests:** A provisional patent application (63/568,783) based on the research described in this manuscript is submitted on 24 March 2024 by the Southern Illinois University Carbondale. The inventors on this patent application are P.K., A.Y.V.-L., M.A.A., S.D.H.-B., and N.A.M. The authors declare that they have no competing interests. **Data and materials availability:** All data needed to evaluate the conclusions in the paper are present in the paper and/or the Supplementary Materials.

Submitted 25 February 2024 Accepted 27 June 2024 Published 2 August 2024 10.1126/sciadv.ado5555